

BROCK UNIVERSITY LIBRARY



3 9157 00929477 1







# Infrared Spectroscopy of Mg-doped $\text{SrRuO}_3$ Thin Films

by

Fatemeh Eftekhari

A THESIS SUBMITTED IN PARTIAL FULFILMENT OF  
THE REQUIREMENTS FOR THE DEGREE OF

MASTER OF SCIENCE

in

The Faculty of Mathematics and Sciences

Department of Physics



BROCK UNIVERSITY

August 21, 2006

2006 © Fatemeh Eftekhari

**JAMES A GIBSON LIBRARY  
BROCK UNIVERSITY  
ST. CATHARINES ON**



In presenting this thesis in partial fulfilment of the requirements for an advanced degree at the Brock University, I agree that the Library shall make it freely available for reference and study. I further agree that permission for extensive copying of this thesis for scholarly purposes may be granted by the head of my department or by his or her representatives. It is understood that copying or publication of this thesis for financial gain shall not be allowed without my written permission.

(Signature) \_\_\_\_\_

Department of Physics

Brock University

St.Catharines, Canada

Date \_\_\_\_\_



# Abstract

The reflectance of thin films of magnesium doped  $\text{SrRuO}_3$  (Mg-SRO) produced by pulsed laser deposition on  $\text{SrTiO}_3$  (100) substrates has been measured at room temperature between 100 and  $7500\text{ cm}^{-1}$ . The films were chosen to have wide range of thickness, stoichiometry and electrical properties. As the films were very thin (less than 300 nm), and some were insulating the reflectance data shows structures due to both the film and the substrate. Hence, the data was analyzed using Kramers-Kronig constrained variational fitting (VDF) method to extract the real optical conductivity of the Mg-SRO films. Although the VDF technique is flexible enough to fit all features of the reflectance spectra, it seems that VDF could not eliminate the substrate's contribution from film conductivity results. Also the comparison of the two different programs implementing VDF fitting shows that this technique has a uniqueness problem.

The optical properties are discussed in light of the measured structural and transport properties of the films which vary with preparation conditions and can be correlated with differences in stoichiometry. This investigation was aimed at checking the VDF technique and also getting answer to the question whether  $\text{Mg}^{2+}$  substitutes in to Ru or Sr site. Analysis of our data suggests that  $\text{Mg}^{2+}$  goes to Ru site.



# Contents

Abstract . . . . .	ii
Contents . . . . .	iii
List of Tables . . . . .	vi
List of Figures . . . . .	vii
Acknowledgements . . . . .	x
1 Introduction . . . . .	1
2 Optical Properties of Solids . . . . .	5
2.1 Interaction of Light with an Optical Medium . . . . .	5
2.2 Drude-Lorentz Model . . . . .	8
2.3 Frequency Dependence of Drude-Lorentz Model . . . . .	12
2.3.1 Lorentz Model with a single Oscillator ( $\epsilon_\infty \approx 1$ ) . . . . .	12
2.3.2 Drude Model . . . . .	15



---

2.4	Kramers-Kronig Relations . . . . .	18
<b>3</b>	<b>Basics of Optical Data Fitting . . . . .</b>	<b>20</b>
3.1	Non-Linear Modeling . . . . .	21
3.1.1	Levenberg-Marquardt Algorithm . . . . .	21
3.1.2	Confidence Limit . . . . .	25
3.2	Determination of the Dielectric Functions . . . . .	27
3.2.1	KK-Constrained Variational Fitting Method . . . . .	27
3.2.2	Anchor Frequencies . . . . .	30
<b>4</b>	<b>Experimental Method . . . . .</b>	<b>32</b>
4.1	Spectrometer . . . . .	32
4.2	Sample Chamber . . . . .	36
4.3	Detectors . . . . .	36
<b>5</b>	<b>Optical Properties of Mg-doped SrRuO<sub>3</sub> Thin Films . . . . .</b>	<b>38</b>
5.1	Samples . . . . .	38
5.2	Reflectance . . . . .	38
5.3	Optical Conductivity . . . . .	41
5.3.1	Drude-Lorentz Simple Model For $\epsilon_f$ . . . . .	42
5.3.2	VDF Fitting For $\epsilon_f$ . . . . .	42
5.4	Weaknesses of VDF . . . . .	48



---

5.4.1	Uniqueness of Solution . . . . .	48
5.4.2	Inability to Remove Substrate Contribution . . . . .	51
5.5	Vibrational Properties . . . . .	52
6	Conclusions . . . . .	59
A	Preparing $\text{Sr}_{1-x}\text{Mg}_{x+y}\text{Ru}_{1-y}\text{O}_{3-\delta}$ thin films . . . . .	61
B	$\text{Sr}_{1-x}\text{Mg}_{x+y}\text{Ru}_{1-y}\text{O}_{3-\delta}$ Samples Characterization . . . . .	63
B.1	RBS: Stoichiometry and Thickness . . . . .	63
B.2	Electrical and magnetic properties . . . . .	63
C	Rutherford Back Scattering Method [29, 30] . . . . .	68
	Bibliography . . . . .	70



# List of Tables

4.1	Different Optical Components for different working frequency ranges .	34
5.1	Thin films Samples Characterization . . . . .	39
5.2	Drude-Lorentz parameters for $\epsilon_f$ determined by reflectivity spectra fitting of $\text{SrMg}_y\text{Ru}_{1-y}\text{O}_{3-\delta}$ . . . . .	45
5.3	IR active modes for cubic SRO calculated using full potential LMTO linear response [20] . . . . .	54
A.1	Experimental raw material mass ratios for making $\text{SrRu}_{0.85}\text{Mg}_{0.15}\text{O}_3$ [26]	61
A.2	Thin film growth parameters . . . . .	62



# List of Figures

1.1	Infrared-reflectivity data and Lorentzian fits for bulk $\text{Cd}_{1-x}\text{Zn}_x\text{Te}$ . The primary CdTe- and ZnTe- like peaks are indicated. Arrows mark some of the additional small peaks or shoulders that are related to dopants [11]. . . . .	2
2.1	Classical model of the bound electrons in an atom {after [12]}. . . . .	6
2.2	Classical model of a polar molecule, in which the spring represents the molecular bond between oppositely charged atoms {after [12]}. . . . .	7
2.3	(a) Reflectivity as a function of wavenumber in the Lorentz Model, (b) Frequency dependence of the real and imaginary parts of the complex dielectric function, (c) Real and imaginary part of the conductivity calculated from the dielectric function. . . . .	14
2.4	(a) Reflectivity as a function of wavenumber in the Drude Model, (b) Frequency dependence of the real and imaginary parts of the complex dielectric function, (c) Real and imaginary part of the conductivity calculated from the dielectric function. . . . .	16
3.1	The block diagram of Levenberg-Marquardt technique . . . . .	24



---

3.2	Dielectric functions with (a) Lorentz lineshape (b) Triangular lineshape [1] . . . . .	29
3.3	Variational dielectric function [1] . . . . .	30
4.1	The Michelson interferometer . . . . .	33
4.2	General layout of the optical table (taken from [24]) . . . . .	35
5.1	Reflectance spectra of the Mg-SRO and pure SRO thin films at room temperature. . . . .	40
5.2	A comparison of a VDF fit with simple Drude-Lorentz fit to the re- flectance of sample DM30. . . . .	43
5.3	Optical conductivity of Mg-SRO samples, assuming $\epsilon_f$ can be modeled using DL Model. These curves were generated using the parameters of table 5.2. . . . .	44
5.4	Optical conductivity of Mg-SRO samples determined using REFFIT.EXE	46
5.5	Optical conductivity of Mg-SRO samples determined using ORFITZ.EXE	47
5.6	A comparison of obtained (a) fitted reflectivity (b) conductivity from two different codes. . . . .	49
5.7	A comparison of obtained (a) refractive index (b)extinction index from two different codes. . . . .	50
5.8	A Comparison of Optical conductivity of DM31 for three different as- sumed thickness. The actual film thickness is $900 \pm 20\text{\AA}$ . . . . .	51



---

5.9	The optical phonon modes of the cubic perovskite structure $\text{ABO}_3$ : (a) stretching; (b) bending; (c) inactive; (d) external. Two internal modes (stretching and bending) and one external mode are IR active [22]. . . . .	53
5.10	IR active mode frequency $\omega_0$ , scattering rate $\gamma$ and bonding strength $\omega_p^2$ versus composition (X) for Ru-O stretch mode. Triangle shape represents DM31 film. . . . .	57
5.11	IR active mode frequency $\omega_0$ , scattering rate $\gamma$ and bonding strength $\omega_p^2$ versus composition (X) for Mg-O stretch mode in $\text{SrMg}_y\text{Ru}_{1-y}\text{O}_{3-\delta}$ thin films. Triangle shapes represent DM31 film. . . . .	58
B.1	RBS spectrum of all Mg-SRO samples. The arrow in each panel indicates the edge associated with Ru at the back of the film. . . . .	64
B.2	Temperature dependent remanent magnetization of all samples . . . . .	66
B.3	Temperature dependent DC resistivity of the five Mg-SrO samples used in the reflectance measurement . . . . .	67



# Acknowledgements

I would like to thank my supervisor, Dr. Crandles for the opportunities he gave me and providing me with his help, guidance, patience and time.

I would like to acknowledge Prof. S. Bose for his helpful theoretical calculation. I also thank Dr. G.V. Sudhakar for helping us with the experiments.

My special thanks to my husband, Saeed, for his love, support and patience during my studies. Ill never forget all of his help and encouragements throughout my programming days.

And finally, I also would like to thank my parents for their unending love and support in every stage of my life.



# Chapter 1

## Introduction

One of purposes of performing optical spectroscopy in a given material is to determine its complex dielectric function  $\varepsilon(\omega) = \varepsilon_1(\omega) + i\varepsilon_2(\omega)$  (or, equivalently, the complex optical conductivity) in the largest possible photon energy range. The dielectric function will, then, give information about the electronic structure of the material, of other excitations occurring in the material, and possibly the mechanism driving transitions to states such as superconductivity or magnetism. It is based on the interaction of an external field with the electric dipole moment of the sample.

The first goal of this thesis is to check the technique of finding dielectric function  $\varepsilon(\omega)$  or optical conductivity  $\sigma(\omega)$  by fitting reflectance spectra using KK-constrained variational dielectric fitting (so-called VDF) method which was proposed by A. Kuzmenko [1]. In principle this technique allows extraction of  $\sigma(\omega)$  from reflectance data of very thin films where both substrate and film produce structure in the spectrum. A program was written to implement VDF fitting for both single crystals and thin films.

The second goal of the thesis is to use VDF fitting to determine  $\sigma_1(\omega)$  in Mg-doped  $\text{SrRuO}_3$  thin films. It is desirable to explore the  $\text{Sr}_{1-x}\text{Mg}_{x+y}\text{Ru}_{1-y}\text{O}_{3-\delta}$  (Mg-SRO) system to further the understanding of doped  $\text{SrRuO}_3$  (SRO). Previous uncertainty in chemical analysis leaves open the possibility that Mg is substituting into both Sr



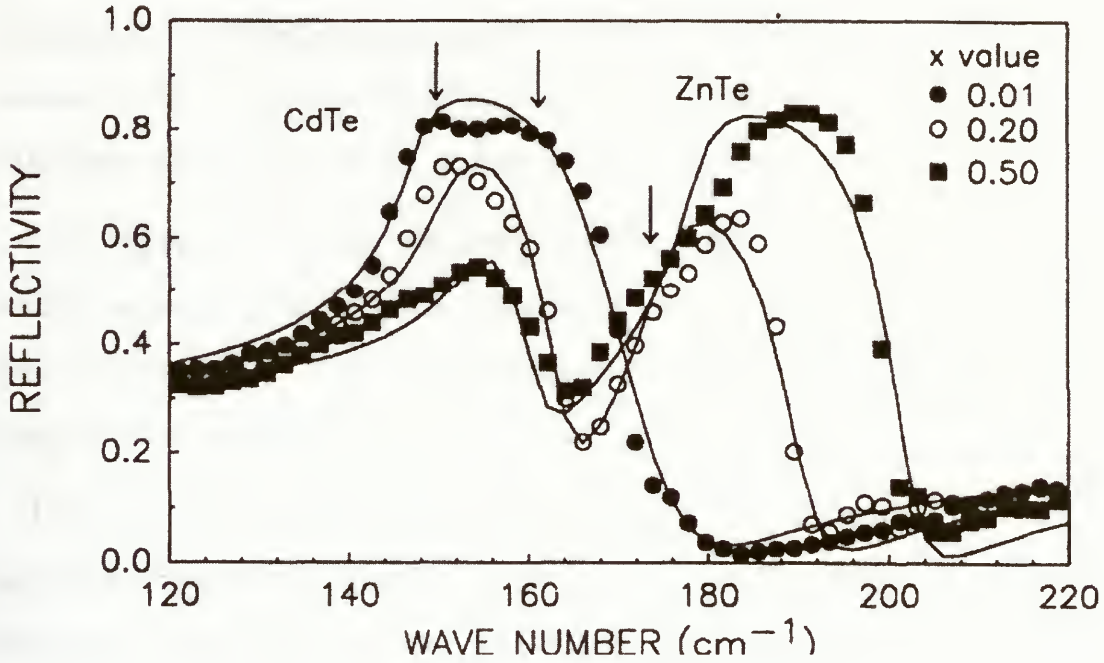


Figure 1.1: Infrared-reflectivity data and Lorentzian fits for bulk  $\text{Cd}_{1-x}\text{Zn}_x\text{Te}$ . The primary CdTe- and ZnTe- like peaks are indicated. Arrows mark some of the additional small peaks or shoulders that are related to dopants [11].

and Ru sites. IR spectroscopy can probe site substitution via splitting of vibration modes in optical spectra.

Previous work on the optical reflectance of doped materials report that dopants create additional structures on or near the material's primary peaks (see figure 1.1). For example, when Zn is doped into CdTe in  $\text{Cd}_{1-x}\text{Zn}_x\text{Te}$ , the primary ZnTe-like peak starts as a shoulder near  $175 \text{ cm}^{-1}$  for  $x = 0.01$  and grows to prominence as  $x$  increases.

$\text{SrRuO}_3$  (SRO) is a pseudocubic perovskite and an itinerant ferromagnet with a



Curie temperature of  $\sim 160$  K [2, 3]. Most reports on bulk materials indicate that it is orthorhombic with lattice parameters of  $a \cong 5.557$  Å,  $b \cong 5.53$  Å and  $c \cong 7.856$  Å [4]; however, there are also reports of different phases, particularly, a tetragonal phase with lattice parameters of  $a \cong b \cong 5.62$  Å and  $c \cong 7.81$  Å [5].

SRO is one of the highly conductive metallic oxides. Transport analysis shows metallic behavior up to 1000 K in spite of a very short coherence length of 10 Å at room temperature [6]. It also has good thermal conductivity and stability and high resistance to chemical corrosion [7].

Recently, epitaxial thin films of  $\text{SrRuO}_3$  have been widely studied because of its important electrical and magnetic properties, such as high remnant magnetization and large magneto-optical constant [8] which make this material very useful for making various electronic and optic devices. Furthermore, because of its high metallic conductivity and chemical stability it is of potential use in microelectronic applications.

Another remarkable property of this material is the effect of Sr or Ru site substitution. The different behavior in transport as well as in magnetic measurements reveals a clear separate mechanism responsible for the properties observed. The following previous research has been done on perturbation of  $\text{SrRuO}_3$  :

**$\text{Sr}_{1-x}\text{Ca}_x\text{RuO}_3$**  Ferromagnetism persists with up to 65% substitution of  $\text{Ca}^{2+}$  for  $\text{Sr}^{2+}$ . Also it remains metallic over the whole range of  $x$  [9].

**$\text{SrRu}_{1-x}\text{Ti}_x\text{O}_3$**  Ferromagnetism destroyed with a bit over 20% substitution of  $\text{Ti}^{4+}$  for  $\text{Ru}^{4+}$  and it becomes insulator at low temperatures for large values of Ti substitution [9].



**SrRu<sub>1-x</sub>Mg<sub>x</sub>O<sub>3</sub>(polycrystalline)** Mg substitution the Ru site causes ferromagnetism with insulating transport properties. As long as the amount of Mg is less than  $x = 0.15$ , there is no significant variation in structure compared to SrRuO<sub>3</sub> [10].

We present our thesis in three major chapters. Chapter 2 will discussed the principles of Drude-Lorentz (DL) model, a widely used model for describing the response of the optical media to an electromagnetic wave, and also the base of the VDF method, which is explained in chapter 3. Chapter 4 deals with the experimental method of reflectance spectroscopy. Studying and analyzing the measured reflectance of the thin films in order to check the VDF technique and also understand the vibrational modes of Mg-SRO films make up chapter 5.



## Chapter 2

# Optical Properties of Soilds

### 2.1 Interaction of Light with an Optical Medium

The classical model of light propagation was explained by using Maxwell's theory of electromagnetic waves and the introduction of the concept of the dipole oscillator. In the dipole oscillator model [12] there are three major types of oscillators within a medium, each with their own characteristic resonant frequencies.

- **Atomic Oscillators:** At optical frequencies the most important contribution is from bound electrons within the atoms. The idea is to consider atoms as oscillating dipoles. It is assumed that the electron is held in a stable orbit with respect to the nucleus with a spring which represents the restoring force for small displacements from the equilibrium. The negatively charged electron cloud and the positively charged nucleus form an electric dipole with a magnitude proportional to their separation. Figure 2.1 is illustrates schematically the dipole oscillator model. There are several dipoles within every atom, so a given atom has many transition frequencies. The natural resonant frequency  $\omega_0$  of the atomic dipole is determined by their mass and the magnitude of the



restoring force experienced for small displacement from following formula.

$$\omega_0 = \sqrt{\frac{K_s}{\mu}} \quad (2.1)$$

where  $\mu$  is reduced mass and  $K_s$  is spring constant.

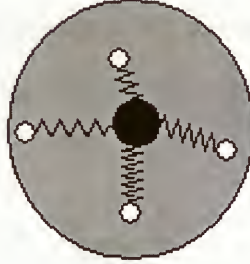


Figure 2.1: Classical model of the bound electrons in an atom {after [12]}.

Once the AC electric field is applied, it exerts forces on the electrons and nucleus, which are very small compared to the binding forces that hold the electrons to the nucleus, and drives oscillations of the system at frequency  $\omega$ . If  $\omega$  coincides with one of the natural frequencies of the atom, then there is a resonance phenomenon. It means very large amplitude oscillations with transferring energy from the external wave to the atom. Hence the atom absorbs energy from the light wave if  $\omega = \omega_0$ . Once the atom has been excited, it can return to the ground state either by a series of transitions (in which case the absorbed photon energy is converted to heat) or by re-radiating photons in all directions, which are incoherent with each other. This implies the reduction of the energy flow in the beam direction, in other words absorption. If  $\omega$  does not match up with any of the natural resonant frequencies, then the atoms will not absorb, and the medium will be transparent and the wave will propagate with smaller



velocity compared to free space.

- **Vibrational Oscillators:** In ionic optical media, the atoms are positively and negatively charged, and can vibrate about their equilibrium separation. These vibrations produce an oscillating electrical dipole which will radiate electromagnetic waves at the resonant frequencies. Alternatively, the molecule will interact with the electric field of a light wave through the forces exerted on the charged atoms.

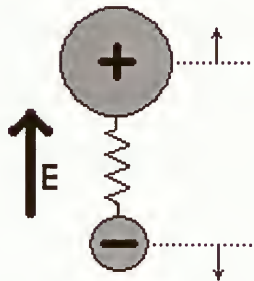


Figure 2.2: Classical model of a polar molecule, in which the spring represents the molecular bond between oppositely charged atoms {after [12]}.

Figure 2.2 shows a schematic illustration of a classical polar molecule. A polar molecule is one in which the electron charge cloud that forms the bond sits closer to one of the atoms than to the other. Since reduced mass is larger in comparison with atomic oscillators, so molecular vibration will occur at lower frequencies. In a crystal solid formed from the condensation of polar molecules the atoms are arranged in an alternating sequence of positive and negative ions. The dipole oscillations are associated with lattice vibrations, and they occur at frequencies in the infrared spectral region in which one can see the strong



absorption lines in the spectra.

- **Free electron Response:** The electronic and vibrational dipoles considered above are both examples of bound oscillators. Metal and doped semiconductors, by contrast, contain significant numbers of free electrons which do not experience any restoring forces when they are displaced. One can model as Lorentz oscillator with  $\omega_0 = 0$ . This type of oscillator is responsible for the principal optical properties of metals.

The simplest microscopical model to describe the response of the optical medium to an electromagnetic field ( $\vec{E}$ ) is the Drude-Lorentz model. This model is a system of harmonic oscillators coupled via electrostatic dipole-dipole interactions.

## 2.2 Drude-Lorentz Model

In this model [13] we consider an electron (of mass  $m$  and charge  $e$ ) bound to the nucleus in a similar way a small mass can be bound to a large one. In solids, oscillating dipoles can lose their energy by interaction with the phonons which have been thermally excited in the crystal. Thus we model the electronic dipoles as damped harmonic oscillators. On the other hand, the electric field of the light wave induces forced oscillations of the atomic dipole through the driving forces exerted on the electrons. With all of these considerations, the equation of motion for an electron is

$$m\ddot{\mathbf{r}} + m\gamma\dot{\mathbf{r}} + m\omega_0^2\mathbf{r} = -e\mathbf{E} \quad (2.2)$$

where  $\gamma$  is the damping rate, and  $E$  is  $E_{loc}$ .



Fourier transforming this differential equation gives

$$m\mathbf{r}(\omega) (-\omega^2 - i\omega\gamma + \omega_0^2) = -e\mathbf{E}(\omega) \quad (2.3)$$

Thus

$$\mathbf{r}(\omega) = \frac{e\mathbf{E}(\omega)}{m(\omega^2 - \omega_0^2 + i\omega\gamma)} \quad (2.4)$$

The displacement of the electrons from their equilibrium position produces a time varying dipole moment  $\mathbf{P}(t)$ , the magnitude of the dipole moment per electron is given by

$$P(t) = -e\mathbf{r}(t) \quad (2.5)$$

This gives a resonant contribution to the macroscopic polarization (dipole moment per unit volume) of the medium. If  $N$  is the number of atoms per unit volume then

$$\mathbf{P}(\omega) = -\frac{Ne^2}{m} \frac{1}{(\omega^2 - \omega_0^2 + i\omega\gamma)} \mathbf{E}(\omega) \quad (2.6)$$

The electric displacement  $\mathbf{D}$  of the medium is related to the electric field  $\mathbf{E}$  and polarization  $\mathbf{P}$  through:

$$\mathbf{D} = \epsilon_0\mathbf{E} + \mathbf{P} \quad (2.7)$$

On the other hand, the dielectric function is defined through the relation:

$$\mathbf{D} = \epsilon\mathbf{E} \quad (2.8)$$

then by combining eqns 2.6-2.8 we obtain

$$\epsilon(\omega) = 1 + \frac{\omega_p^2}{(\omega_0^2 - \omega^2) - i\omega\gamma} \quad (2.9)$$

where  $\omega_p^2$  is plasma frequency, which is defined as

$$\omega_p^2 = \frac{4\pi Ne^2}{m} \quad (2.10)$$



A plane wave of electromagnetic radiation propagating in a sample is both absorbed and shifted in phase. Thus the response of the crystal to an optical probe is a complex function. Taking the real and imaginary parts of equation 2.9, we get

$$\varepsilon_1(\omega) = 1 + \frac{\omega_p^2(\omega_0^2 - \omega^2)}{(\omega_0^2 - \omega^2)^2 + \omega^2\gamma^2} \quad (2.11)$$

$$\varepsilon_2(\omega) = \frac{\omega_p^2\gamma\omega}{(\omega_0^2 - \omega^2)^2 + \omega^2\gamma^2} \quad (2.12)$$

From Maxwell equations, the relation between the complex conductivity and the complex dielectric constant is defined as

$$\varepsilon(\omega) = 1 + \frac{4\pi i}{\omega}\sigma(\omega) \quad (2.13)$$

Using equation 2.13 the optical conductivity in this model is found to be:

$$\sigma(\omega) = \frac{\omega_p^2}{4\pi} \frac{\omega}{i(\omega_0^2 - \omega^2) + \omega\gamma} \quad (2.14)$$

with its real and imaginary parts are as follows:

$$\sigma_1(\omega) = \frac{\omega_p^2}{4\pi} \frac{\omega^2\gamma}{(\omega_0^2 - \omega^2)^2 + \omega^2\gamma^2} \quad (2.15)$$

$$\sigma_2(\omega) = -\frac{\omega_p^2}{4\pi} \frac{\omega(\omega_0^2 - \omega^2)}{(\omega_0^2 - \omega^2)^2 + \omega^2\gamma^2} \quad (2.16)$$

Furthermore, the refractive index of a medium is related to its dielectric function  $\varepsilon(\omega)$  by the standard result derived from Maxwell's equations :

$$N = \sqrt{\varepsilon} \quad (2.17)$$



Since  $\varepsilon$  is complex, then  $N$  is complex too,  $N = n + i\kappa$ . By analogy with equation 2.17, it shows that their real and imaginary parts are related to each other through:

$$\varepsilon_1 = n^2 - \kappa^2 \quad (2.18)$$

$$\varepsilon_2 = 2n\kappa \quad (2.19)$$

and

$$n = \frac{1}{\sqrt{2}} \left( \varepsilon_1 + (\varepsilon_1^2 + \varepsilon_2^2)^{\frac{1}{2}} \right)^{\frac{1}{2}} \quad (2.20)$$

$$\kappa = \frac{1}{\sqrt{2}} \left( -\varepsilon_1 + (\varepsilon_1^2 + \varepsilon_2^2)^{\frac{1}{2}} \right)^{\frac{1}{2}} \quad (2.21)$$

The reflectivity depends on both  $n$  and  $\kappa$  and is given by

$$R = \left| \frac{N - 1}{N + 1} \right|^2 = \frac{(n - 1)^2 + \kappa^2}{(n + 1)^2 + \kappa^2} \quad (2.22)$$

Free electrons are not bound and the correspondent optical conductivity is obtained by setting  $\omega_0 = 0$ . This gives rise to the well known Drude model often used to describe the low frequency response of metals.

To analyze experimental data, one usually takes the sum model dielectric function which is the combination of one Drude peak and various Lorentz oscillators:

$$\varepsilon(\omega) = \varepsilon_\infty - \frac{\omega_p^2}{\omega(\omega + i\gamma)} + \sum_j \frac{\omega_{p,j}^2}{(\omega_{0,j}^2 - \omega^2) - i\omega\gamma_j} \quad (2.23)$$

where the additional parameter  $\varepsilon_\infty$  is introduced, which is the contribution of oscillators where  $\omega_{0,j} \gg \omega$ , the frequency range of interest.



## 2.3 Frequency Dependence of Drude-Lorentz Model

The interaction of an electronic system with the electromagnetic field leads to an absorption process. In the sum model each absorption process is considered to be a Lorentz oscillator. A Lorentz oscillator is described by three parameters:

1. Resonance frequency  $\omega_j$
2. Damping frequency  $\gamma_j$
3. Plasma frequency  $\omega_{p,j}$

The damping frequency is a measure of how easily the Lorentz oscillator transfers energy to its environment and plasma frequency is a parameter related to the strength of the coupling of the oscillator to the external electromagnetic radiation.

### 2.3.1 Lorentz Model with a single Oscillator ( $\varepsilon_\infty \approx 1$ )

For the Lorentz model four regimes with distinctively different spectral characteristics are of importance: a low frequency range at which the material does not absorb, the spectral range close to the center frequency  $\omega_0$  at which electrons are excited and thus absorption dominate, a range of high reflectivity for  $\omega_0 < \omega < \omega_p$ , and the transparent regime for large frequencies  $\omega > \omega_p$  [13].

**Low frequency range:** At frequencies  $\omega < (\omega_0 - \gamma)$ , the light is not reflected, but it is transmitted with almost no attenuation. In this region  $\kappa \simeq 0$ , thus the



relation between absorption coefficient  $\alpha$  and  $\kappa$  ( equation 2.24) implies that there is also no absorbtion at low frequencies.

$$\alpha = \frac{2\kappa\omega}{c} \quad (2.24)$$

Also, as it displayed in panel (b) of figure 2.3, at low frequency range, one can approximate  $\varepsilon_1$  with:

$$\varepsilon_1(\omega) \approx \varepsilon_{st} = \varepsilon_{\infty} + \frac{\omega_p^2}{\omega_0^2} \quad (2.25)$$

**Absorption range:** The vicinity of the oscillator frequency  $\omega_0$  is characterized by strong absorption due to the large conductivity  $\sigma_1$ . The width of the absorption range is characterized by the damping rate  $\gamma$ , it is the full width at half of the conductivity maximum. Two extrema of  $\varepsilon_1$  happen at  $\omega_{extr} \simeq \omega_0 \pm \frac{\gamma}{2}$ . As displayed in the figure 2.3, the optical conductivity exhibit strong changes in this region.

**Reflection range:** The third frequency range is  $(\omega_0 + \gamma) < \omega < \omega_p$ . This region is characterized by a high and almost frequency independent reflectivity. As shown in panel (a) of figure 2.3, at the oscillator frequency  $\omega_0$  and at the plasma frequency  $\omega_p$  the curvature of the reflectivity changes. In this region, conductivity drops as

$$\sigma_1(\omega) \propto \frac{\gamma^2}{\omega^2} \quad (2.26)$$

$$\sigma_2(\omega) \propto \frac{\gamma}{\omega} \quad (2.27)$$

Also one can approximate dielectric function with these

$$\varepsilon_1(\omega) \approx \varepsilon_{\infty} - \frac{\omega_p^2}{\omega^2} \quad (2.28)$$

$$\varepsilon_2(\omega) \approx \frac{\gamma\omega_p^2}{\omega^3} \quad (2.29)$$



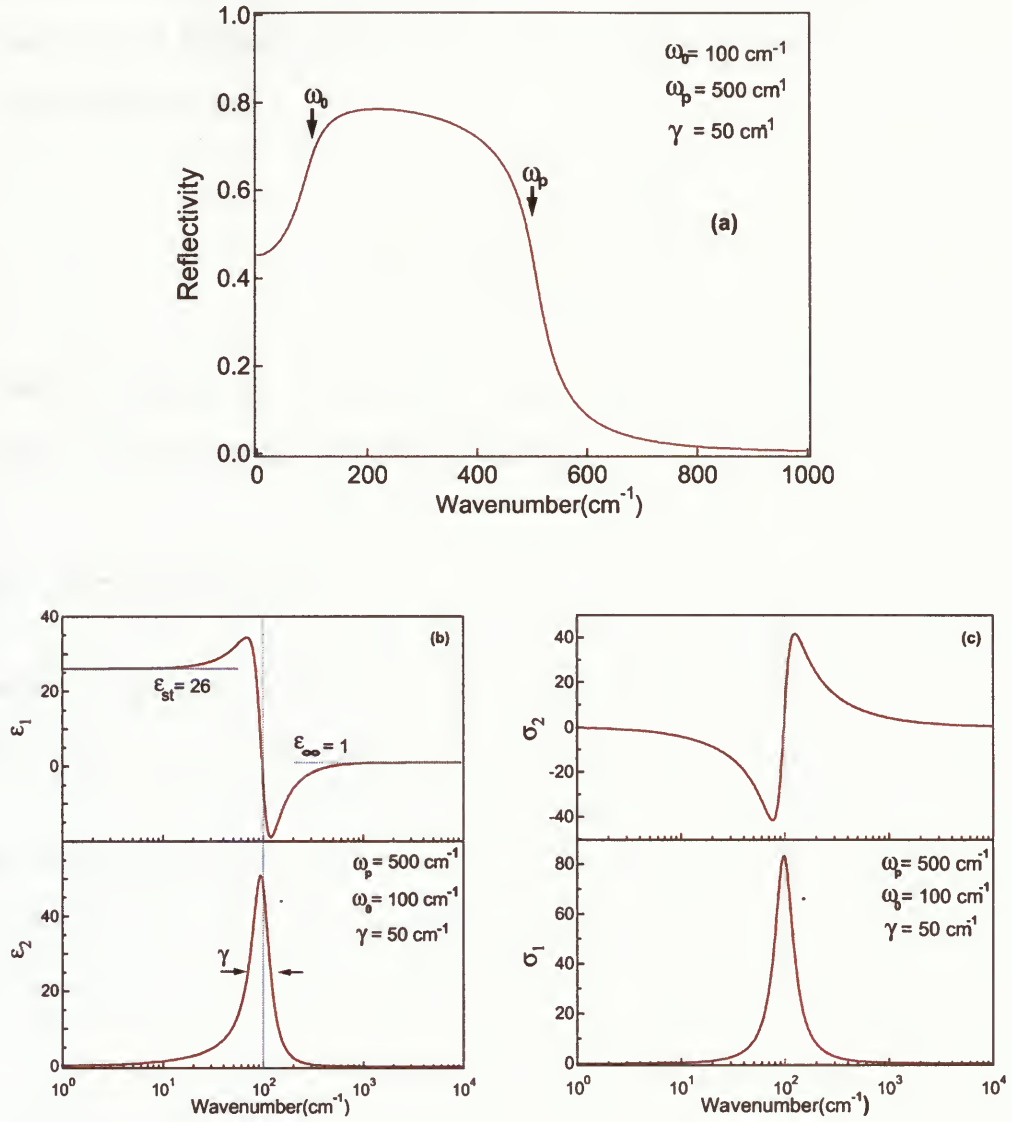


Figure 2.3: (a) Reflectivity as a function of wavenumber in the Lorentz Model, (b) Frequency dependence of the real and imaginary parts of the complex dielectric function, (c) Real and imaginary part of the conductivity calculated from the dielectric function.



**Transparent range:** At frequencies above  $\omega_p$ , transmission is again important.

Same as low frequency range, since  $\kappa$  is small, the reflectivity is dominated by the behavior of  $n(\omega)$ .

$$n \approx \varepsilon_1^{\frac{1}{2}} \approx \varepsilon_\infty - \frac{\omega_p^2}{2\omega^2} \quad (2.30)$$

$$R \approx \frac{(n-1)^2}{(n+1)^2} \approx \frac{\omega_p^4}{16\omega^4} \quad (2.31)$$

At high frequencies  $\omega \gg \omega_p$ ,  $\varepsilon_1(\omega)$  approaches  $\varepsilon_\infty$ , thus reflectivity drops to zero, and the material becomes transparent.

### 2.3.2 Drude Model

For Drude model, three different regimes can be distinguished in the spectra, that each of them have a characteristic optical response different from each other [13].

**Hagen-Rubens regime:** This region is defined by condition  $\omega \ll \gamma$ . In this region the optical properties are mainly determined by the dc conductivity which is defined as:

$$\sigma_{dc} \equiv \sigma_1(\omega = 0) = \frac{\omega_p^2}{4\pi\gamma} \quad (2.32)$$

As can be seen in panel (c) of figure 2.4, in this region  $\sigma_1(\omega) \gg \sigma_2(\omega)$ :

$$\sigma_1(\omega) \approx \sigma_{dc} \quad (2.33)$$

$$\sigma_2(\omega) \approx \sigma_{dc} \frac{\omega}{\gamma} \quad (2.34)$$

For  $\omega \ll \gamma$ , dielectric function approaches:

$$\varepsilon_1(\omega) \approx \varepsilon_\infty - \frac{\omega_p^2}{\gamma^2} \quad (2.35)$$



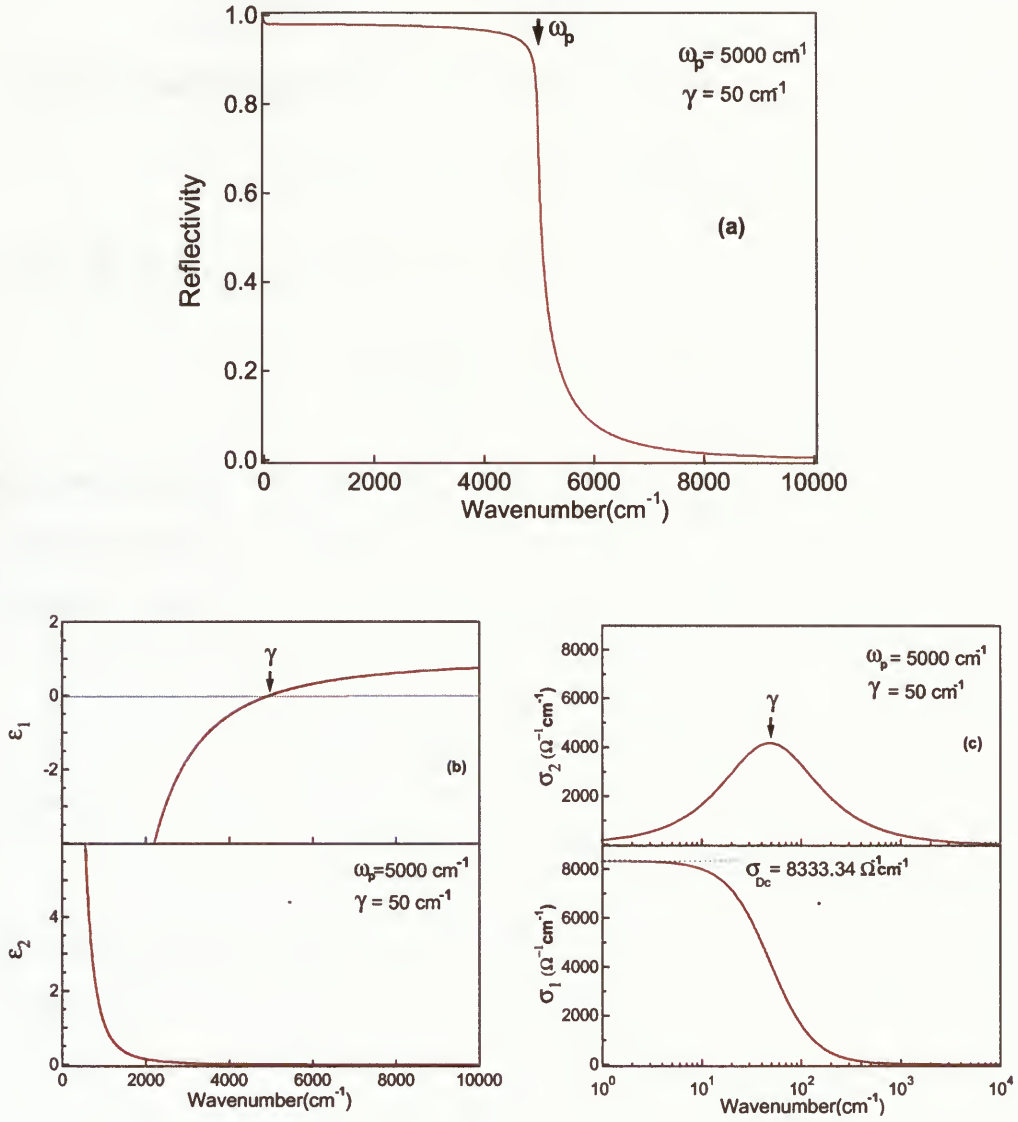


Figure 2.4: (a) Reflectivity as a function of wavenumber in the Drude Model, (b) Frequency dependence of the real and imaginary parts of the complex dielectric function, (c) Real and imaginary part of the conductivity calculated from the dielectric function.



$$\varepsilon_2(\omega) \approx \frac{\omega_p^2}{\gamma\omega} \quad (2.36)$$

For the refractive index both components are equal:

$$n(\omega) = \kappa(\omega) = \left[ \frac{\varepsilon_2(\omega)}{2} \right]^{\frac{1}{2}} = \left( \frac{2\pi\sigma_{dc}}{\omega} \right)^{\frac{1}{2}} \gg 1 \quad (2.37)$$

The reflectivity  $R$  can now be written as

$$R(\omega) \approx \frac{\kappa(\omega) - 1}{\kappa(\omega) + 1} \approx 1 - \left( \frac{8\omega\gamma}{\omega_p^2} \right)^{\frac{1}{2}} \quad (2.38)$$

**Relaxation regime:** For the frequencies which lie in the intermediate spectral range between the scattering rate  $\gamma$  and the plasma frequency  $\omega_p$ , the real optical conductivity can be approximated to

$$\sigma_1(\omega) \approx \frac{\omega_p^2\gamma}{4\pi\omega^2} \quad (2.39)$$

While

$$\varepsilon_1(\omega) \approx -\frac{\omega_p^2}{\omega^2} \quad (2.40)$$

In this regime the reflectivity becomes frequency independent, and it can be written as

$$R(\omega) \approx 1 - \frac{2\gamma}{\omega_p} \quad (2.41)$$

**Transparent regime:** The reflectivity of a metal drops significantly at the plasma frequency, and above  $\omega_p$  the material becomes transparent. In this region, optical conductivity approaches

$$\sigma_1(\omega) \propto \omega^{-2} \quad (2.42)$$

$$\sigma_2(\omega) \propto \omega^{-1} \quad (2.43)$$



For  $\omega \leq \omega_p$ , the extinction  $\kappa$  is approximately  $\frac{1}{2}|\varepsilon_1|$ , while for frequencies  $\omega > \omega_p$ , it vanishes. Consequently the absorption coefficient  $\alpha$  undergoes a sudden decrease near  $\omega_p$ , and hence the medium becomes transparent.

## 2.4 Kramers-Kronig Relations

The physical basis of the Kramers-Kronig relations is the principle of causality. The cause in optical phenomena is the incident electromagnetic wave, and the effect is the response of the crystal, associated with the motion of electrons and nuclei. Due to causality the real part of the dielectric function  $\varepsilon_1(\omega)$  is connected to its imaginary part  $\varepsilon_2(\omega)$  by Kramers-Kronig relations [14], which are:

$$\varepsilon_1(\omega) - 1 = \frac{2}{\pi} \int_0^\infty \frac{\omega'}{(\omega'^2 - \omega^2)} \varepsilon_2(\omega') d\omega' \quad (2.44)$$

$$\varepsilon_2(\omega) = \frac{2}{\pi} \int_0^\infty \frac{\omega}{(\omega^2 - \omega'^2)} \varepsilon_1(\omega') d\omega' \quad (2.45)$$

$\omega$  and  $\omega'$  are real and independent values of the angular frequency.

The Kramers-Kronig relations are non-local in frequency: the real (imaginary) component of response at a certain frequency  $\omega$  is related to the behavior of the imaginary (real) part over the entire frequency range, although the influence of the contributions diminishes as  $(\omega'^2 - \omega^2)$  for larger and larger frequency differences. This global behavior leads to certain difficulties when these relations are used to analyze experimental results which cover only a finite range of frequencies. Certain qualitative statements can, however, be made, in particular when one or the other component of the response function displays a strong frequency dependence near certain frequencies. The KK relations can be used to extract the complex dielectric



---

function from reflectance data [15] taken a single material. On the other hand, we can not use these relations for thin films because of contribution of substrate on overall reflectivity spectra.



# Chapter 3

## Basics of Optical Data Fitting

The calculations were based on the assumption that the measured optical reflectivity can be expressed in terms of the complex frequency dependent dielectric function as

$$\varepsilon(\omega) = \varepsilon_1(\omega) + i\varepsilon_2(\omega)$$

The normal-incident reflectivity for single crystal depends on the dielectric function via formulae 2.18-2.22.

Determining the optical properties of a film deposited on a substrate requires the knowledge of the properties of the substrate. For film-substrate system, the normal-incident reflectivity can be derived from following formulae [13]:

$$R = \left| \frac{r_f + t^2 r_{fs}}{1 + t^2 r_f r_{fs}} \right|^2 \quad (3.1)$$

where

$$r_f = \frac{1 - \sqrt{\varepsilon_f}}{1 + \sqrt{\varepsilon_f}} \quad (3.2)$$

$$r_{fs} = \frac{\sqrt{\varepsilon_f} - \sqrt{\varepsilon_s}}{\sqrt{\varepsilon_f} + \sqrt{\varepsilon_s}} \quad (3.3)$$

$$t = \exp(i \frac{\omega}{c} \sqrt{\varepsilon_f} d) \quad (3.4)$$



$\varepsilon_s$  and  $\varepsilon_f$  are the dielectric function of the substrate and the film, respectively and  $d$  is the film thickness.  $\varepsilon_s$  was taken from literature data [24]. We desire to obtain  $\varepsilon_f$  which will be a non-linear function of several parameters.

## 3.1 Non-Linear Modeling

Suppose, the model to be fitted is

$$y = f(x; \vec{a})$$

which depends nonlinearly on the set of  $M$  unknown parameters  $a_k$ ,  $k = 1, 2, \dots, M$ .

And the  $\chi^2$  merit function is defined as

$$\chi^2(\vec{a}) = \sum_{i=1}^N \left[ \frac{y_i - f(x_i; \vec{a})}{\sigma_i} \right]^2 \quad (3.5)$$

where  $\sigma_i$  is the experimental uncertainty of  $y_i$ . The best-fit parameters are derived by minimization of  $\chi^2$ .

### 3.1.1 Levenberg-Marquardt Algorithm

The Levenberg-Marquardt algorithm (LMA) is the most popular curve-fitting algorithm that provides a numerical solution to the problem that is called *Nonlinear Least Squares Minimization* [16].

LMA can be thought of as a combination of steepest descent and the Gauss-Newton method. When the current solution is far from the correct one, the algorithm behaves like a steepest descent method: slow, but guaranteed to converge. When the current solution is close to the correct solution, it becomes a Gauss-Newton method.



Suppose, the current parameter values are  $a_k$ . To improve the fit, we can shift the parameters by amount of  $\delta a_k$

$$a_k \rightarrow a_k + \delta a_k \quad (3.6)$$

In ‘steepest descent’ (or ‘gradient descent’) method the increments  $\delta a_k$  is determined from

$$\delta a_k = \text{constant} \times \beta_k \quad (3.7)$$

where  $\beta_k$  is the minus-gradient of  $\chi^2$  with respect to the parameters  $a_k$  :

$$\beta_k \equiv -\frac{1}{2} \frac{\partial \chi^2}{\partial a_k} = \sum_{i=1}^N \frac{y_i - f(x_i; a)}{\sigma_i^2} \frac{\partial f(x_i; a)}{\partial a_k} \quad (3.8)$$

In ‘Gauss-Newton method’, finding a minimum is done by means of searching for a zero of the gradient of the function. Newton’s method is very good in the final stage of the iteration, where  $a_k$  is close to optimum ones  $a$ . From Taylor expansion near the current point  $a_k$ ; where  $\mathbf{D} = \nabla^2 \chi^2(a_k)$

$$\chi^2(a) = \chi^2(a_k) + (a - a_k) \cdot \nabla \chi^2(a_k) + \frac{1}{2} (a - a_k) \cdot \mathbf{D} \cdot (a - a_k) \quad (3.9)$$

so

$$\nabla \chi^2(a) = \nabla \chi^2(a_k) + \mathbf{D} \cdot (a - a_k) \quad (3.10)$$

Gauss-Newton method simply involves setting  $\nabla \chi^2(a)$  to zero so that the required step becomes

$$a - a_k = -\mathbf{D}^{-1} \cdot \nabla \chi^2(a_k) \quad (3.11)$$

By defining matrix  $[\alpha] = \frac{1}{2} \mathbf{D}$ ,

$$\begin{aligned} \alpha_{kl} &\equiv \frac{1}{2} \frac{\partial^2 \chi^2}{\partial a_k \partial a_l} \\ &= \sum_{i=1}^N \frac{1}{\sigma_i^2} \left[ \frac{\partial f(x_i; a)}{\partial a_k} \frac{\partial f(x_i; a)}{\partial a_l} - [y_i - f(x_i; a)] \frac{\partial^2 f(x_i; a)}{\partial a_l \partial a_k} \right] \end{aligned} \quad (3.12)$$



the equation 3.11 can be rewritten as the set of linear equations:

$$\sum_{l=1}^M \alpha_{kl} \delta a_l = \beta_k \quad (3.13)$$

In the context of least-squares, the matrix  $[\alpha]$  is called the *curvature matrix*. The term multiplying the second derivative in equation 3.12 is  $[y_i - f(x_i; a)]$ . For a successful model, this term should be the random measurement error of each point. This error can have either sign, and in general it should be uncorrelated with the model. Therefore, the second derivative terms tend to cancel out when summed over  $i$ . So instead of equation 3.12, one can define the  $[\alpha]$  simply as

$$\alpha_{kl} = \sum_{i=1}^N \frac{1}{\sigma_i^2} \left[ \frac{\partial y(x_i; a)}{\partial a_k} \frac{\partial y(x_i; a)}{\partial a_l} \right] \quad (3.14)$$

It is obvious that in equation 3.7, the proportionality constant between  $\beta_k$  and  $\delta a_k$  has the dimension of  $a_k^2$ . To eliminate the dimension, the constant is normalized by  $1/\alpha_{kk}$  (the reciprocal of the diagonal element of  $[\alpha]$ ).

$$\delta a_k = \frac{\text{constant}}{\alpha_{kk}} \beta_k \quad (3.15)$$

Note that the  $\delta a_k$  might be too big, so to avoid this problem, the constant is divided by some nondimensional factor  $\lambda$ , with the possibility of setting  $\lambda \gg 1$  to cut down the step. So 3.15 can be replaced by

$$\delta a_k = \frac{1}{\lambda \alpha_{kk}} \beta_k \quad (3.16)$$

Marquardt's insight provides elegant way to combine equations 3.16 and 3.13. By defining a new matrix  $\alpha'$  as

$$\alpha'_{jj} \equiv \alpha_{jj}(1 + \lambda) \quad (3.17)$$



$$\alpha'_{jk} \equiv \alpha_{jk} \quad (j \neq k)$$

and then replace both 3.13 and 3.16 by

$$\sum_{l=1}^M \alpha'_{kl} \delta a_l = \beta_k \quad (3.18)$$

For large  $\lambda$ , the diagonal components of  $[\alpha']$  become dominant, so equation 3.18 goes over to 3.16. Also when  $\lambda$  gets small and approaches zero as a limit, equation 3.18 goes over to 3.13.

The well-known LM algorithm is shown as a block diagram in figure 3.1.

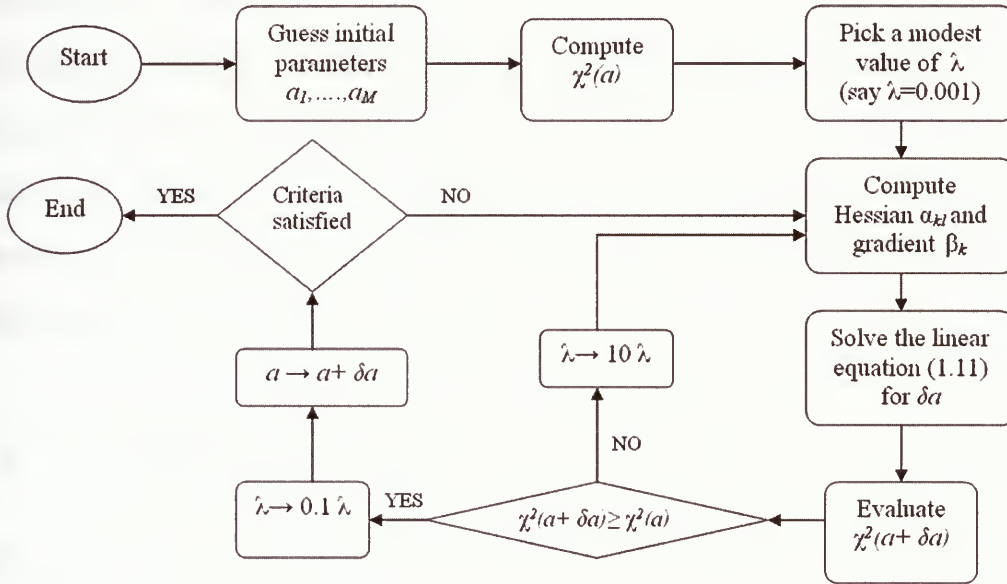


Figure 3.1: The block diagram of Levenberg-Marquardt technique

The minimization process is iterative. Given an initial guess for the set of fitted parameters  $a$ , one starts process with a small value of  $\lambda$  (e.g., 0.001). At every successful iteration,  $\chi_{new}^2 < \chi_{current}^2$ ,  $\lambda$  is reduced by a factor of 10, moving towards



the inverse Hessian regime. Otherwise it retreats to the steepest descent regime by being increased by a factor of 10. When the so-called stop criteria are satisfied, the fitting process stops.

The stop condition is necessary to avoid an endless iteration cycle. Iterating to convergence (to machine accuracy or to the roundoff limit) is generally wasteful and unnecessary since the minimum is at best only a statistical estimate of the parameters  $a$ . So one of the good criteria is putting a condition on amount of changing  $\chi^2$ , means when the absolute reduction of the  $\chi^2$  during the last few (e.g., four) iterations does not exceed a certain threshold (e.g.,  $\delta\chi < 10^{-3}$ ). Also necessary is putting certain limits on the total number of iteration to ensure that the fitting process does not take too long. Another important issue is the computation of  $\alpha_{kl}$  and  $\beta_k$ . In general, one can calculate it numerically. But in this case the computational errors might be considerable, particularly near the minimum point. In our case, since we use Drude-Lorentz model function that it has explicit analytical expression, so the derivatives are calculated analytically.

### 3.1.2 Confidence Limit

Basically, there are always uncertainties in estimated parameters  $a$ . Rather than present all details of the probability distribution of errors in parameter estimation, it is common practice to summarize the distribution in the form of “confidence limits”.

One can define the confidence limit of a parameter  $a_k$  as the largest possible value  $\delta E_k$ , where the shift  $a_k \rightarrow a_{(0)k} + \delta E_k$  does not cause an unrealistic large increase of the chi-square after minimizing with respect to all remaining parameters.



For the observed data set, the value of  $\chi^2$  is a minimum at  $a_{(0)}$ . Call this minimum value  $\chi_{min}^2$ . If the parameter values is perturbed away from  $a_{(0)}$ , then  $\chi^2$  increases. The region within which  $\chi^2$  increases by no more than a set amount  $\Delta\chi^2$  defines some M-dimensional confidence region around  $a_{(0)}$ . From Hessian matrix  $\alpha_{kl}$ , by ignoring the deviations of  $\chi^2(a_1, \dots, a_M)$  near the minimum point  $\chi_{min}^2(a_{(0)1}, \dots, a_{(0)M})$  from the quadratic shape, one can get

$$\chi^2 - \chi_{min}^2 = \sum_{k,l} \alpha_{kl} (a_k - a_{(0)k}) (a_l - a_{(0)l}) \quad (3.19)$$

If  $M$  is the number of fitted parameters and  $p$  is the confidence limit desired (e.g.,  $p=0.68$  or  $p=0.95$ ), then one can find  $\Delta\chi^2$  such that the probability of a chi-square variable with  $M$  degrees of freedom being less than  $\Delta\chi^2$  is  $p$ . For a given  $M$  and  $p$  values,  $\Delta\chi^2$  is determined from following equation [16]

$$Q\left(\frac{M}{2}, \frac{\Delta\chi^2}{2}\right) = 1 - p \quad (3.20)$$

where  $Q(a, x)$  is called incomplete gamma function,

$$Q(a, x) \equiv \frac{\Gamma(a, x)}{\Gamma(a)} \equiv \frac{1}{\Gamma(a)} \int_x^\infty e^{-t} t^{a-1} dt \quad (3.21)$$

If  $\Delta\chi^2$  is chosen as a maximum acceptable difference  $\chi^2 - \chi_{min}^2$ , then after doing some algebra, one can derive

$$\delta E_k = \sqrt{(\Delta\chi^2)(\alpha^{-1})_{kk}} \quad (3.22)$$

where  $(\alpha^{-1})_{kk}$  is the inverse Hessian matrix, that it is called Covariance matrix.



## 3.2 Determination of the Dielectric Functions

Traditionally there are 2 ways to extract  $\varepsilon_1(\omega)$  and  $\varepsilon_2(\omega)$  of studied sample from measured reflectance spectra

- **Kramers-Kronig (KK) relations**[15]: They are accurate and they give us all the details, but they need abroad frequency range that might be hard in some experiments. Also, in a case of thin film system, the method does not work, because of contribution of substrate on overall reflectivity spectra.
- **Least-square Fitting**: In this technique we are using simple dielectric function model such as Drude-Lorentz oscillators. The reflectance data is fit to a model dielectric function equation 2.23 using 2.18-2.22. In comparison, this technique has some advantages over KK. First, it does not need wide frequency range and second, all of its parameters are easily interpreted. But because of its limitation it cannot fit all the details of reflection spectra.

### 3.2.1 KK-Constrained Variational Fitting Method

Kuzmenko [1] suggests the KK-constrained variational fitting method which is a combination of the two above mentioned approaches. This fitting process is done in two steps. Initially, the experimental spectrum is fitted with a very limited model  $\varepsilon_{mod}(\omega)$ .

The conventional model for  $\varepsilon_{mod}(\omega)$  is Drude-Lorentz oscillators formula 2.23, in which each term is a lorentzian oscillator with four adjustable parameters:  $\varepsilon_\infty$ ,  $\omega_{0,j}$ ,  $\omega_{p,j}$  and  $\gamma_j$ . The unbound oscillators (conductivity electrons) are described by Drude terms, where  $\omega_{0,j} = 0$ .



If  $\varepsilon_{mod}(\omega)$  describes the major features of experiment spectra then we can go to the next step which is adding the variational function  $\varepsilon_{var}(\omega)$  to perform the final data fitting.

$$\varepsilon(\omega) = \varepsilon_{mod}(\omega) + \varepsilon_{var}(\omega) \quad (3.23)$$

The second step actually is a limiting case of the multi-oscillator fitting. In this technique we consider a dense enough mesh of anchor frequency points  $\omega_1 \dots \omega_N$ , which are not the same as the set of experimental frequencies  $\omega_1^{exp} \dots \omega_{Nexp}^{exp}$  and we distribute them in a way that every anchor point corresponds to at least one experimental points. One separate narrow function for  $\varepsilon_2$ , the absorptive part of the optical response, is placed at each anchor frequency (e.g.  $\omega_{0,i} = \omega_i$ ) to deliver spectral weight everywhere in the spectral range. Moreover, the  $i$ -th function should be narrow enough to provide spectral weight only in the closest neighborhood of  $\omega_i$ , thus we set its width to

$$\gamma_i = \frac{(\omega_{i+1} - \omega_{i-1})}{2} \quad (3.24)$$

So in this way we get a dense set of narrow functions, sitting at fixed anchor frequencies. It is essential to optimize the oscillators lineshape. As can seen in figure 3.2, in Lorentzian line shape for  $\varepsilon_2$  at low and high frequencies, there are two extended tails, which interfere with other oscillators. To avoid interference of functions, it is better to have a lineshape function which is non-zero only inside a small region adjacent to  $\omega_i$ . A **triangular profile** can be one of the best ones.

$$\varepsilon_{2,i}^{\Delta}(\omega) = \begin{cases} (\omega - \omega_{i-1})/(\omega_i - \omega_{i-1}) & \text{if } \omega_{i-1} < \omega \leq \omega_i \\ (\omega_{i+1} - \omega)/(\omega_{i+1} - \omega_i) & \text{if } \omega_i < \omega < \omega_{i+1} \\ 0 & \text{otherwise} \end{cases} \quad (3.25)$$



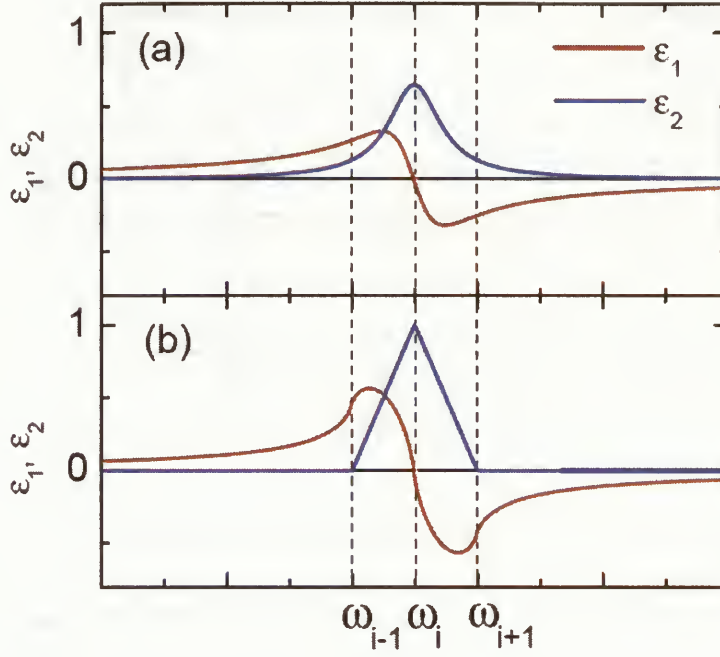


Figure 3.2: Dielectric functions with (a) Lorentz lineshape (b) Triangular lineshape [1]

By KK transformation, the real part can be achieved.

$$\varepsilon_{1,i}^{\Delta}(\omega) = \frac{1}{\pi} \left[ \frac{g(\omega, \omega_{i-1})}{\omega_i - \omega_{i-1}} - \frac{(\omega_{i+1} - \omega_{i-1})g(\omega, \omega_i)}{(\omega_i - \omega_{i-1})(\omega_{i+1} - \omega_i)} + \frac{g(\omega, \omega_{i+1})}{\omega_{i+1} - \omega_i} \right] \quad (3.26)$$

where

$$g(x, y) \equiv (x + y) \ln |x + y| + (x - y) \ln |x - y| \quad (3.27)$$

So the variational dielectric function can be found as a linear superposition of functions sitting at fixed anchor frequencies  $\omega_i$ .

$$\varepsilon_{var} = \sum_{i=2}^{N-1} A_i \varepsilon_i^{\Delta}(\omega) \quad (3.28)$$



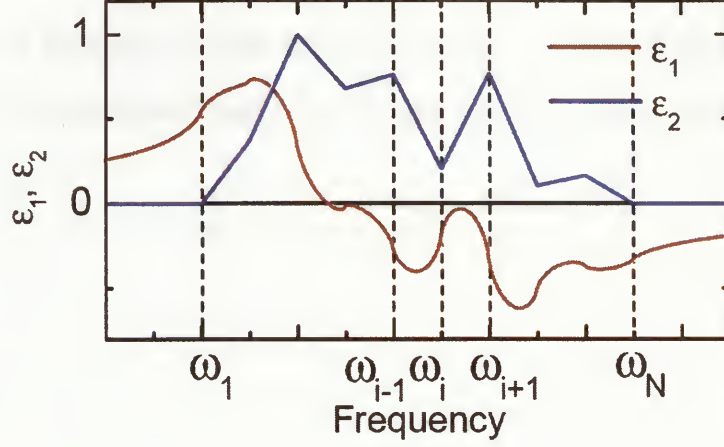


Figure 3.3: Variational dielectric function [1]

where we define the end points,  $A_1 = A_N = 0$ . The coefficients  $A_i$  are like free parameters which are kept adjustable during variational fitting.

As can see in figure 3.3, the imaginary part of  $\varepsilon_{var}$  is a superposition of several triangular functions  $\varepsilon_{2,i}^\Delta$  centered at anchor frequencies, where  $\varepsilon_{1,i}^\Delta$  is the exact KK transform of that.

### 3.2.2 Anchor Frequencies

One of the important issues is the mesh of anchor frequencies. Basically, the number of anchor frequencies should not be too large. First, because of increasing calculation time and secondly an excessive flexibility may cause numerical instability. On the other hand, it should be dense enough to enable the VDF to fit all fine details. Kuzmenko suggests that the optimal number of anchor frequencies is two times smaller than the number of experimental frequencies, in which every anchor point correspond



to at least one experimental point.

A program to extract the dielectric function from reflectance data was written implementing KK-constrained variational fitting for both single crystal and thin film systems.



# Chapter 4

## Experimental Method

In reflectance spectroscopy, a sample is exposed to electromagnetic radiation and the intensity of reflected radiation, is measured as a function of its frequency. The optical reflectance is defined as the ratio of the intensity of the beam reflected from sample to that of the beam incident on the sample .

The system consists of three major components:

- Light Source (Interferometer)
- Sample Cryostat
- Detector

Through the use of different light sources, beamsplitters, detectors, and windows, different frequency ranges are achieved.

### 4.1 Spectrometer

A Brüker IFS 66v/S spectrometer modified for reflectance measurement was employed. The Brüker works as a Michelson interferometer. Figure 4.1 shows a layout for a Michelson Interferometer.



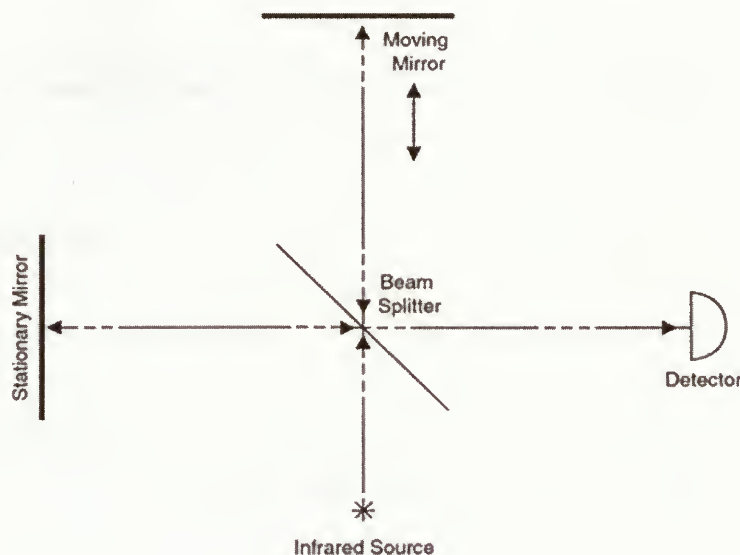


Figure 4.1: The Michelson interferometer

One measures the intensity as a function of position of the moving mirror. This is called an interferogram. A Fourier transform of the interferogram gives the power spectra.

As mentioned before, different frequency ranges are achievable by using various optical components. These are listed in table 4.1.

There is an optical table inside of the Brüker which redirect the light from the spectrometer to the sample chamber. The general layout of the optical table is shown in figure 4.2. Through rotation of a plane mirror by using a step motor, user can change the light path from sample to reference. Also an aperture is placed on the light path in order to control the relative intensity reaching the detector. During the experiment the whole chamber of Brüker is under vacuum.



Table 4.1: Different Optical Components for different working frequency ranges

Component	Type	Working Range ( $\text{cm}^{-1}$ )
BeamSplitter	50 $\mu\text{m}$ Mylar	10-55
	6 $\mu\text{m}$ Mylar with Ge	60-650
	Ge on KBr	370-7500
Light Source	Hg Lamp (FIR)	4-700
	Globar (Mid-IR)	30-7500
	NIR/VIS Tungsten Lamp	4000-30000
Detector	(4.2 K) Bolometer	50-700
	MCT	450-5000
Windows	Polypropylene	30-700
	KBr	370-20000



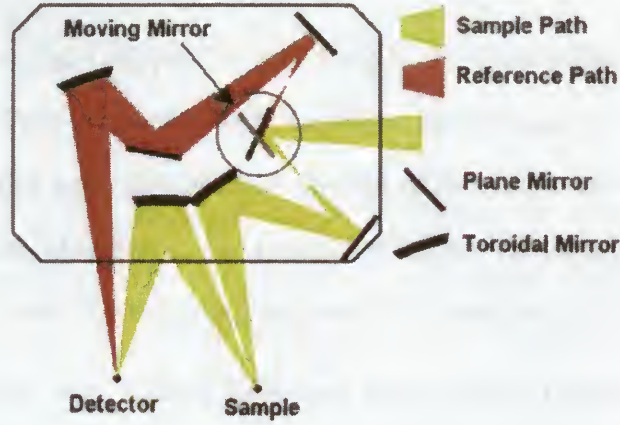


Figure 4.2: General layout of the optical table (taken from [24])

The IR light coming from a source is incident on the measured sample  $I_{Sample}(\omega)$ .  $I_{Reference}(\omega)$  is measured for the independent reference path and corrects for any signal drifts, that can occur during the experiment.

For deriving absolute reflectance, we should coat the sample with some material like gold. This coating procedure corrects possible scattering effects and any unwanted scattering due to surface roughness or sample shape. The amount of gold used is small enough to maintain the same surface topology of the sample. Gold is used here because of its high reflectivity in the FIR and the negligible temperature dependence of its  $R(\omega)$ . Once the power spectra of the coated sample and reference are determined, one can find the absolute reflectance from following formula

$$R_{abs} = \frac{I_{sample}}{I_{Reference}} \times \frac{I_{Reference}}{I_{gold-coatedsample}} \times R_{gold}$$



## 4.2 Sample Chamber

The sample chamber is a rigid support for the sample. It is separated from the optical system with an appropriate window which should be chosen depend on the spectrum being measured. Samples were mounted on the tip of a brass cone which is fixed on the side of a copper block attached in the sample chamber. Although not used during this thesis work, this allows for the temperature of the sample to be varied.

Gases exist in the air can absorb light and reduce light intensity reaching the sample, and subsequently the detector. Hence we pumped out the the sample chamber with turbo pump to maintain the pressure of nearly  $4 \times 10^{-8}$  Torr. Another reason for providing such a low pressure within the sample chamber is to ensure that a high quality gold layer can be deposited on the sample. For making gold film, the gold loops wrapped around a tungsten filament that is adjusted on a flap that can be rotational in front of the sample. At the appropriate time, a flap swings in front of sample, and a current causes the filament to heat-up beyond the melting point of gold. So by thermal evaporation, gold is deposited on the sample's surface.

## 4.3 Detectors

Two different detectors were used for the reflectance measurement. At low frequencies, a bolometer was employed due to its high sensitivity in the frequency range of  $50 \text{ cm}^{-1}$  to  $700 \text{ cm}^{-1}$ . Bolometers are essentially resistance thermometers arranged for response to radiation, which measures the amount of radiation falling upon it by measuring changes in resistance produced by heating due to the radiation.



For frequency range between  $450\text{ cm}^{-1}$  to  $5000\text{ cm}^{-1}$ , we used MCT (HgCdTe) detector which is a photoconductive detector. In a photoconductive detector an electric potential is applied across the absorbing region and causes a current to flow in proportion to the light power falling upon it.

Both of detectors are just working at low temperatures. To achieve the required working temperature for the bolometer, we were using liquid helium and for the MCT, we adjusted it by liquid nitrogen.

In our experiment, the far-infrared and mid-infrared reflectivity were measured at room temperature with a Fourier transform spectrometer Bruker at near normal incidence with the spectral resolution  $5\text{ cm}^{-1}$ . Two detectors (Bolometer and MCT), IR sources (Hg lamp and Globar) and beam splitters (Mylar  $6\mu$  and KBr) were used in the different spectral ranges. The radiation was un-polarized; since the samples are almost cubic, polarization effects are small.



## Chapter 5

# Optical Properties of Mg-doped SrRuO<sub>3</sub> Thin Films

### 5.1 Samples

Several thin films that were previously prepared [17], used for this optical measurement. As seen in table 5.1, they were chosen to have wide range of thickness, stoichiometry and electrical properties. Preparation and characterization details can be found in the Appendices.

### 5.2 Reflectance

Reflectivity spectra for several thin film samples of pure SRO or Mg-doped SRO grown on SrTiO<sub>3</sub> substrates (STO) were measured at room temperature at near normal incidence with the spectral resolution 5 cm<sup>-1</sup> as discussed in chapter 4. Figure 5.1 illustrates the reflectivity spectra of Mg-SRO and pure SRO thin film samples.

Figure 5.1(a) compares the reflectance of Mg-doped SRO (DM31) with pure SRO. Both samples have approximately the same thickness, but their transport properties



Table 5.1: Thin films Samples Characterization

Sample	Stoichiometry		$\sigma(\Omega^{-1}cm^{-1})$	
	$\pm 0.02$ Sr, Ru, Mg	Thickness Å	at 300 K	M(emu/g)
	$\pm 0.1$ O	$\pm 20$ Å	$\pm 2\%$	$\pm 2\%$
SRO	SrRuO <sub>3</sub>	850	3300	-
DM34	SrMg <sub>0.05</sub> Ru <sub>0.95</sub> O <sub>2.75</sub>	1800	2600	5
DM31	SrMg <sub>0.13</sub> Ru <sub>0.87</sub> O <sub>2.65</sub>	900	200	3
DM33	SrMg <sub>0.13</sub> Ru <sub>0.87</sub> O <sub>2.85</sub>	3000	1300	5.5
DM29	SrMg <sub>0.17</sub> Ru <sub>0.83</sub> O <sub>2.9</sub>	2400	590	5.5
DM30	SrMg <sub>0.22</sub> Ru <sub>0.78</sub> O <sub>2.9</sub>	1700	450	6

are completely different. The pure SRO sample is a metal and Mg-doped sample DM31 is an insulator. By comparing samples spectra with substrate's (STO) spectrum, it is found that the two dips at 170 and 470  $cm^{-1}$  are due to substrate's contribution. In both sample's spectra, it can be seen that there is a structure at 580  $cm^{-1}$  (indicated by red arrows), which corresponds to Ru-O stretch mode [18]. Note that in addition to the peak at 580  $cm^{-1}$ , there are new features near 350  $cm^{-1}$  and 670  $cm^{-1}$  in Mg-doped spectrum (indicated by green arrows), which are absent in pure SRO reflectance. By comparing STO reflectance to Mg-SRO spectra, it was found out that the features at 175, 545  $cm^{-1}$  are caused by phonon modes of STO substrate.

Figure 5.1(b) shows the reflectance of samples DM29 and DM30. These samples have approximately the same  $\sigma_{DC}$ , but different thicknesses. As expected, with



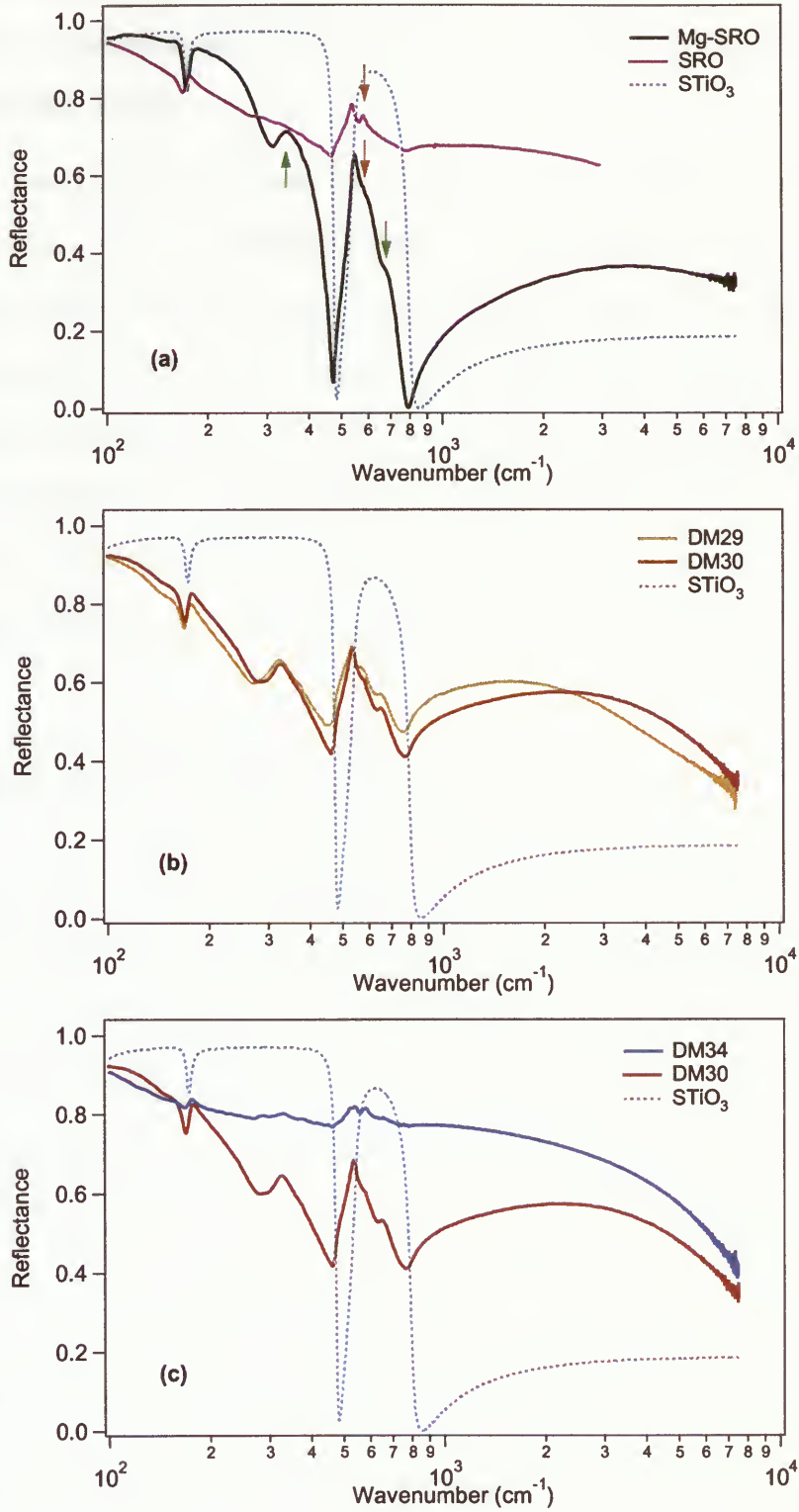


Figure 5.1: Reflectance spectra of the Mg-SRO and pure SRO thin films at room temperature.



decreasing film thickness the response of the STO substrate become more distinguishable in reflectance spectra, and one can see that the STO features are more prominent in the thinner film DM30.

In addition to the film thickness, the conductivity of the films also affects the contribution of substrate in reflectance spectra. It is due to the fact that the skin depth, which is the distance to which incident electromagnetic radiation penetrates, is larger for poor conductors. This effect is clearly seen in figure 5.1(c) where the reflectance of samples DM34 and DM30 are displayed. Both samples have approximately the same thickness but different  $\sigma_{DC}$ . DM34 spectra has high metallic reflectance, in contrast DM30 reflectivity curve has more prominent phonon peaks like an ionic insulator. One can easily observe that the STO peaks are weaker in film DM34.

### 5.3 Optical Conductivity

During the progress of thesis, it was discovered that a program implementing VDF fitting, called REFITT.EXE, was available on the web [19]. Instead of abandoning the program, which was almost complete (ORFITZ.EXE), it was decided to compare the results of these programs.

Hence the real optical conductivity of the SRO and Mg-SRO thin films was determined from equations 3.1-3.4 three ways.

1. Assuming that the film dielectric function  $\epsilon_f$  would be modeled using a simple Drude-Lorentz model. This is the approach of A.F. Santander-Syro [21].
2. Using VDF fitting via REFITT.EXE written by Kuzmenko.



3. Using VDF fitting via ORFITZ.EXE written by the author of this thesis.

### 5.3.1 Drude-Lorentz Simple Model For $\epsilon_f$

As shown in figure 5.2, in general, the DL reflectivity curve seems agree well with the measured reflectivity spectra but there are still some features that DL fitting could not reproduce them. It is interesting to see that using VDF led to better fit result.

Figure 5.3 shows the optical conductivity spectra  $\sigma_1(\omega)$  were obtained using DL fitting of reflectivity spectra. On the y axis, the DC values, measured directly using the Van der Pauw technique, were marked as colored squares. It is certainly interesting to see that the low frequency optical conductivity results are consistent with DC measurements. The Drude-Lorentz parameters determined by least-square fitting are listed in table 5.2. This table will be discussed in greater detail later.

Note the systematic shift of a midinfrared peak to higher frequencies with decreasing the DC conductivity of samples. This behavior is interesting, but will not be discussed in the thesis.

### 5.3.2 VDF Fitting For $\epsilon_f$

The fitting process was done in two steps. Initially the reflectivity was fitted by conventional Drude-Lorentz dielectric function for  $\epsilon_f$  (DL Fitting), and then KK-constrained variational fitting (VDF) was performed. As seen in figure 5.2, the VDF technique is flexible enough to fit all features of the reflectance spectra. In figures 5.4 and 5.5 the optical conductivity spectra of thin film samples, found by KK-constrained variational fitting method, are displayed. These plots reveals the Ru-O bending mode



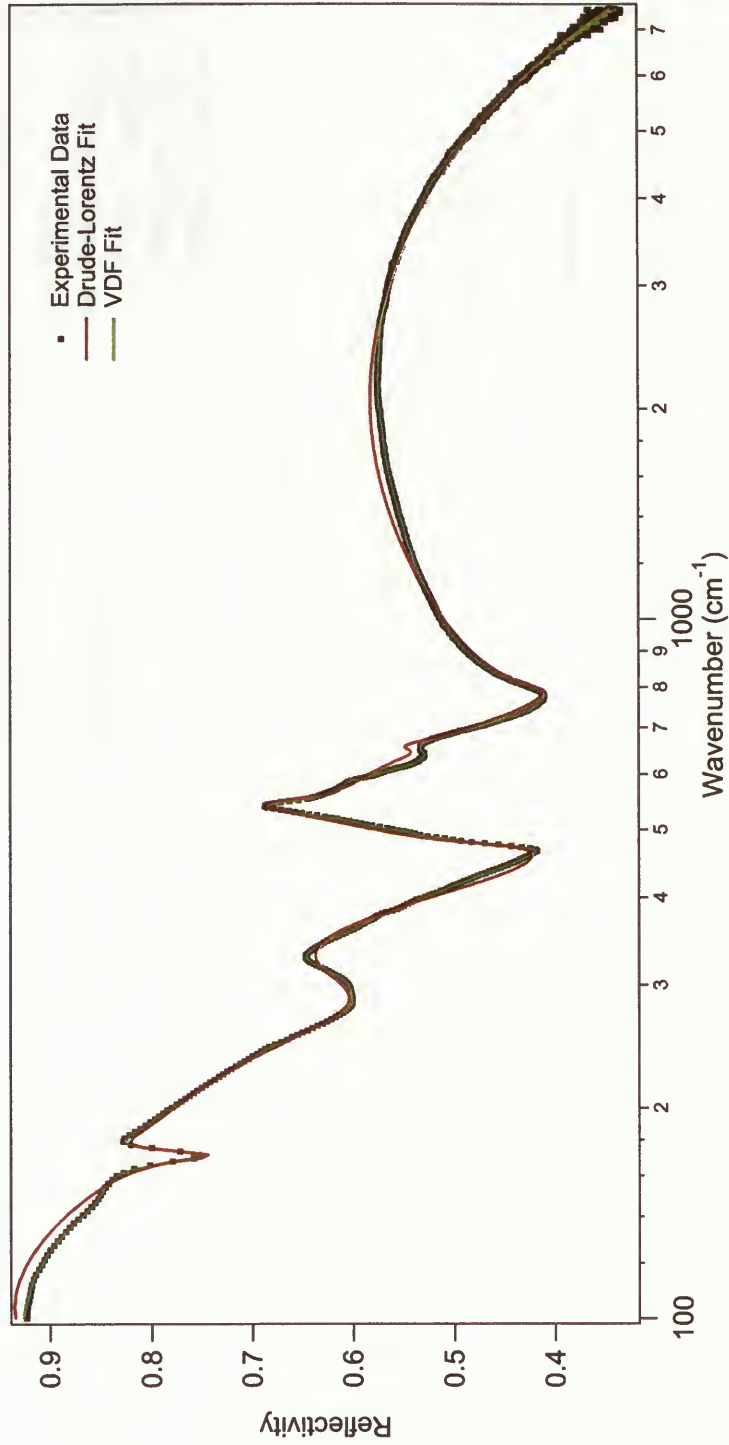


Figure 5.2: A comparison of a VDF fit with simple Drude-Lorentz fit to the reflectance of sample DM30.



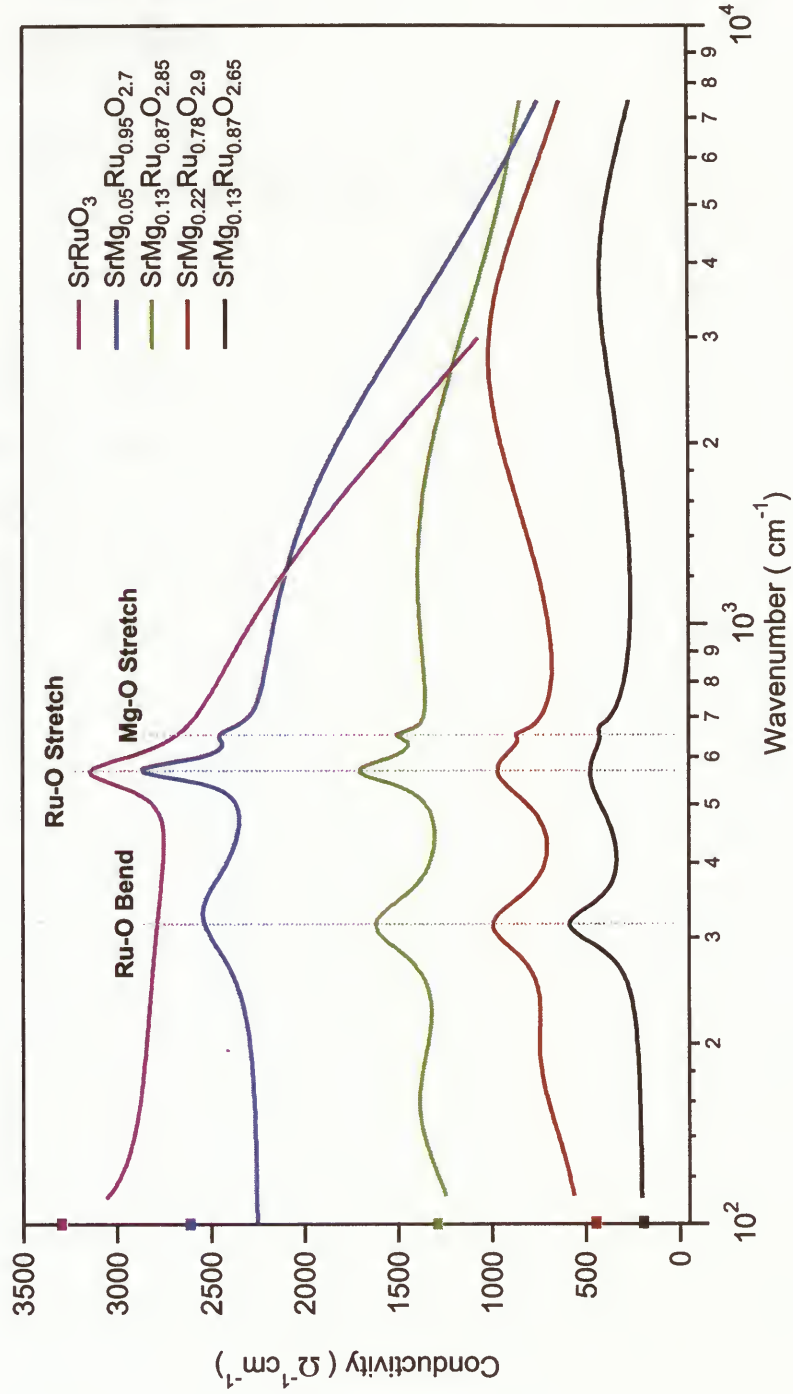


Figure 5.3: Optical conductivity of Mg-SRO samples, assuming  $\epsilon_f$  can be modeled using DL Model. These curves were generated using the parameters of table 5.2.



Table 5.2: Drude-Lorentz parameters for  $\epsilon_f$  determined by reflectivity spectra fitting of SrMg<sub>y</sub>Ru<sub>1-y</sub>O<sub>3- $\delta$</sub> 

Sample		Drude	Bend	Bend	Ru-O Stretch	Mg-O Stretch	MIR band Contribution	$\epsilon_\infty$
SRO*	$\omega_0(\text{cm}^{-1})$	0			578		211	4.99
x=0	$\omega_p(\text{cm}^{-1})$	10843			1306		18372	
	$\gamma(\text{cm}^{-1})$	1400			52		3793	
DM34	$\omega_0(\text{cm}^{-1})$	0	211		572	654	2720	6.09
x=0.05	$\omega_p(\text{cm}^{-1})$	15422	4623		1356	721	22361	
	$\gamma(\text{cm}^{-1})$	2360	460		51	57	10196	
DM33	$\omega_0(\text{cm}^{-1})$	0	155	316	570	654	5883	3.65
x=0.13	$\omega_p(\text{cm}^{-1})$	12789	1586	1530	1324	472	44037	
	$\gamma(\text{cm}^{-1})$	2646	134	93	69	27	44308	
DM29	$\omega_0(\text{cm}^{-1})$	0	156	316	570	654	5018	3.95
x=0.17	$\omega_p(\text{cm}^{-1})$	7108	1424	1703	1662	432	29947	
	$\gamma(\text{cm}^{-1})$	2273	130	125	136	38	18371	
DM30	$\omega_0(\text{cm}^{-1})$	0	186	316	570	654	2828	3.55
x=0.22	$\omega_p(\text{cm}^{-1})$	23704	1525	1487	2033	325	13317	
	$\gamma(\text{cm}^{-1})$	20673	160	92	176	25	5300	
DM31	$\omega_0(\text{cm}^{-1})$	0		315	565	672	4075	11.1
x=0.13	$\omega_p(\text{cm}^{-1})$	4898		1187	1987	334	12804	
	$\gamma(\text{cm}^{-1})$	2000		66	257	37	7223	

\* least-square fitting converge to having another oscillator.



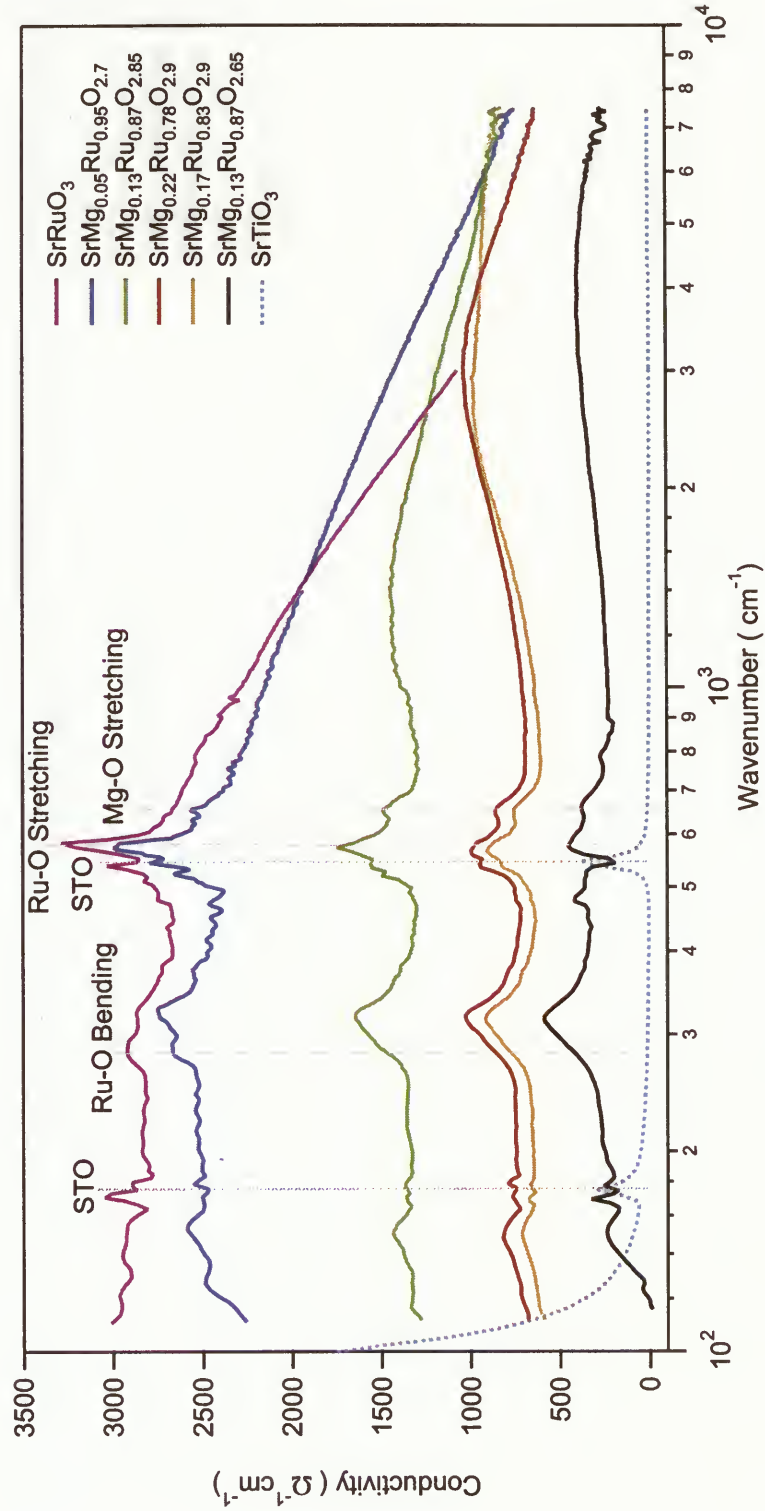


Figure 5.4: Optical conductivity of Mg-SRO samples determined using REFFIT.EXE



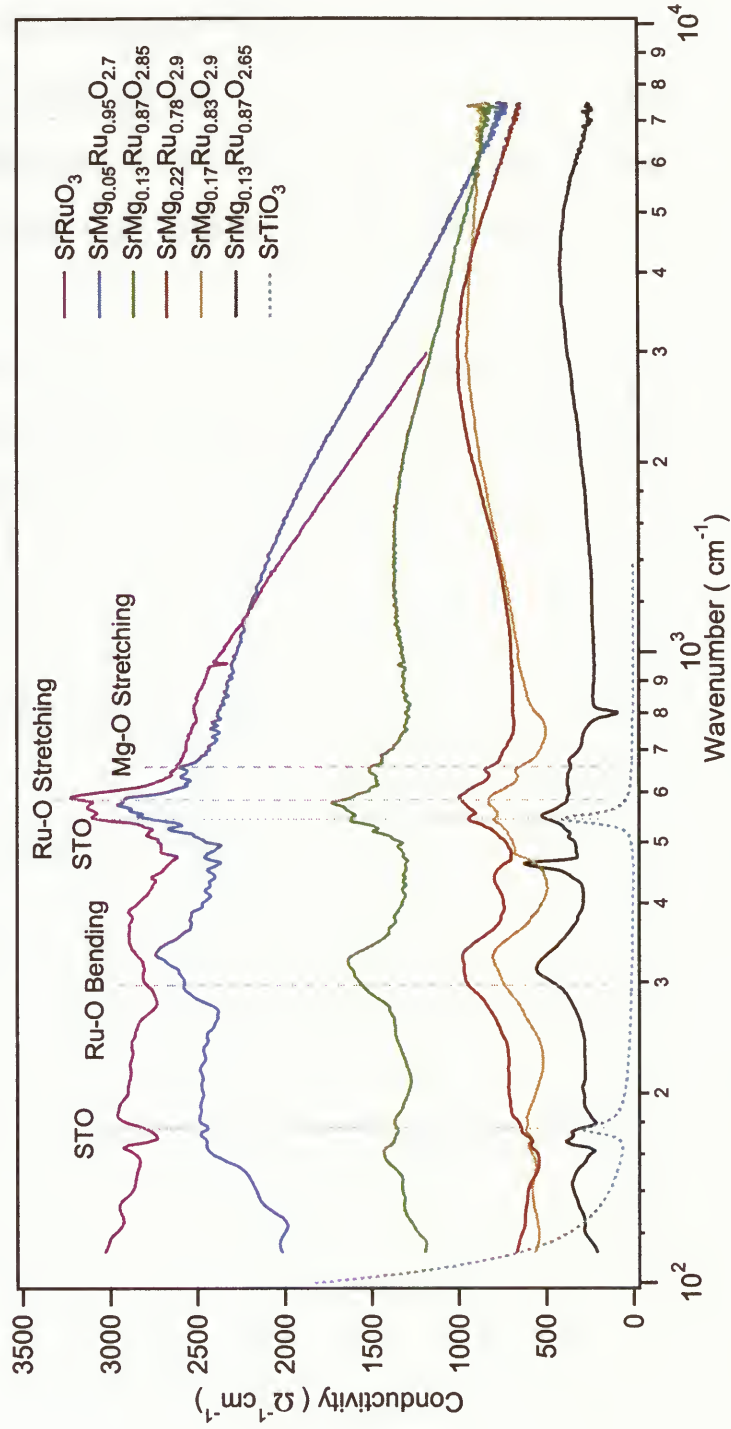


Figure 5.5: Optical conductivity of Mg-SRO samples determined using ORFITZ.EXE



exit in pure SRO (near 300 cm<sup>-1</sup>). Note that DL fitting did not show this. Note also that the VDF fitting reveals splitting of bending modes.

In both conductivity graphs obtained from programs (ORFITZ and REFFIT),  $\sigma_{DC}$  of samples decreases, the MIR feature moves to higher frequencies. Furthermore, the low frequency optical conductivity from REFFIT program matches up to ORFITZ results and  $\sigma_{DC}$ .

Both programs provide the same number of phonon bands and their frequencies are not significantly different. Although, by comparing SrMg<sub>0.22</sub>Ru<sub>0.78</sub>O<sub>2.9</sub> reflectance in both graph 5.4 and 5.5, one can find out an extra peak at 440 cm<sup>-1</sup> in ORFITZ results.

## 5.4 Weaknesses of VDF

### 5.4.1 Uniqueness of Solution

Comparison of the two different programs shows that VDF fitting has a uniqueness problem. Note in figure 5.6(a) that the fits to the experimental reflectance data were equally good. However their conductivity results are slightly different figure 5.6(b). That is because reflectance depends on combination of the real and imaginary part of refractive index, equation 2.22; if at some frequency frequency  $n_{REFFIT}$  is smaller than  $n_{ORFITZ}$ , as in figure 5.7(a), at that same frequency  $\kappa_{REFFIT}$  is bigger than  $\kappa_{ORFITZ}$ , figure 5.7(b), in a way that both of them produce the same value of reflectance.

Despite the uniqueness problem, the presence of vibrational modes at 580 cm<sup>-1</sup>, 670 cm<sup>-1</sup> and several near 300cm<sup>-1</sup> cannot be disputed. The movement of the MIR



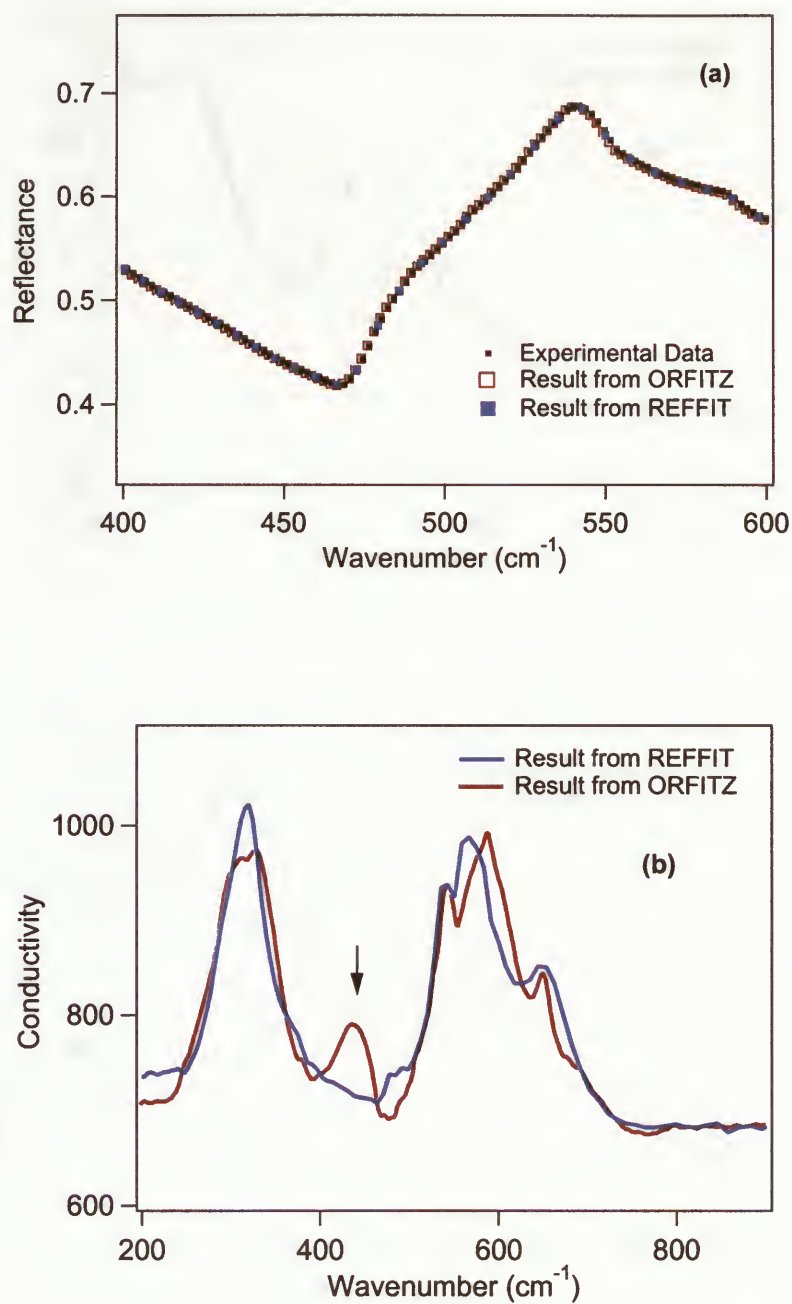


Figure 5.6: A comparison of obtained (a) fitted reflectivity (b) conductivity from two different codes.



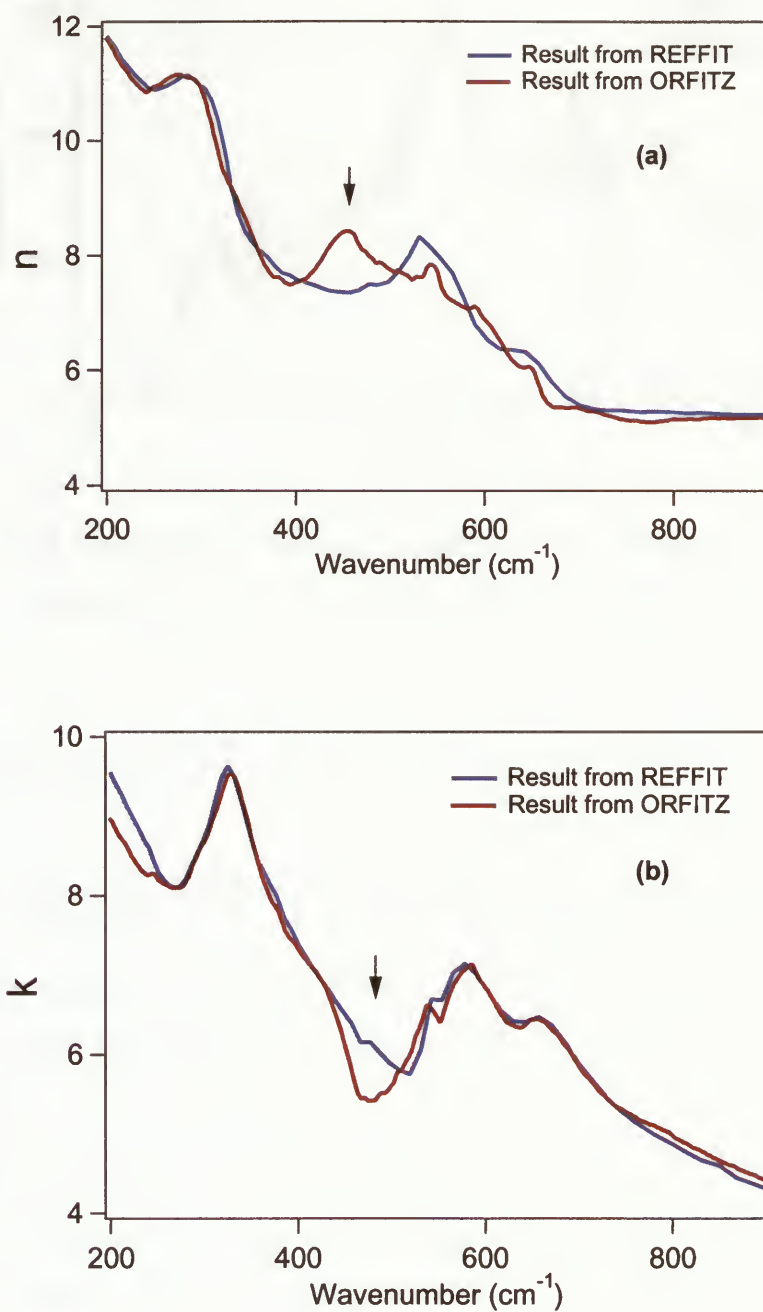


Figure 5.7: A comparison of obtained (a) refractive index (b)extinction index from two different codes.



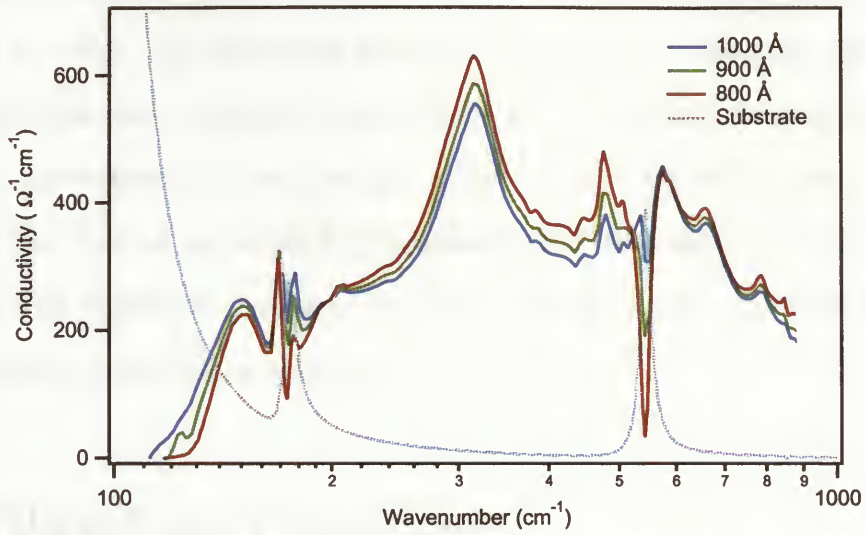


Figure 5.8: A Comparison of Optical conductivity of DM31 for three different assumed thickness. The actual film thickness is  $900 \pm 20 \text{ \AA}$ .

band to higher frequencies as  $\sigma_{DC}$  decreases is also clear.

#### 5.4.2 Inability to Remove Substrate Contribution

By looking at figure 5.8, it was seen that the structures in the far-infrared range are caused not only by peaks in the film conductivity but also by the phonon lines of the substrate.

VDF could not eliminate substrate's contribution from film conductivity results. As seen in the figure 5.8, by assuming different film thickness, a substrate mode's features change more significantly in comparison to film's peaks.



A literature dielectric function [24] was assumed for SrTiO<sub>3</sub> substrate, which may be subject to error. The measured films were deposited on polished substrate but the dielectric function of polished and unpolished crystals may be slightly different this may be the reason that the substrate contribution could not be totally removed. Measuring the  $R(\omega)$  of annealed STO substrate and then using annealed substrate surface for film deposition might be helpful to totally remove phonon lines of the substrate in film conductivity spectra.

## 5.5 Vibrational Properties

The cubic (ABO<sub>3</sub>) perovskite structure has three infrared active modes of symmetry  $F_{1u}$  and one optically inactive mode of symmetry  $F_{2u}$  [22]. The inactive  $F_{2u}$  mode can become optically active due to distortions of the crystal lattice from the ideal cubic structure [23]. The remaining three  $F_{1u}$  modes are IR active, corresponding to the vibrational motion in which the B-O bond distance is modulated (the stretching mode), the B-O bond angle is modulated (the bending mode) or the translational motion of the A atoms with respect to BO<sub>3</sub> (the external mode), as illustrated in figure 5.9. Two factors influence phonon frequency, the interatomic potential and the mass of the atoms involved in the vibration.

In order to assign the modes in vibrational spectra a full potential LMTO linear response was performed by Dr. S. Bose [20]. It predicts three infrared active modes for SRO in cubic perovskite structure, listed in table 5.3. The cubic perovskite has less atoms per unit cell (five atoms) in compare to orthorhombic perovskite which has 20 atoms per unit cell. So in cubic perovskite, 15 phonon modes (5triple degeneracy) are



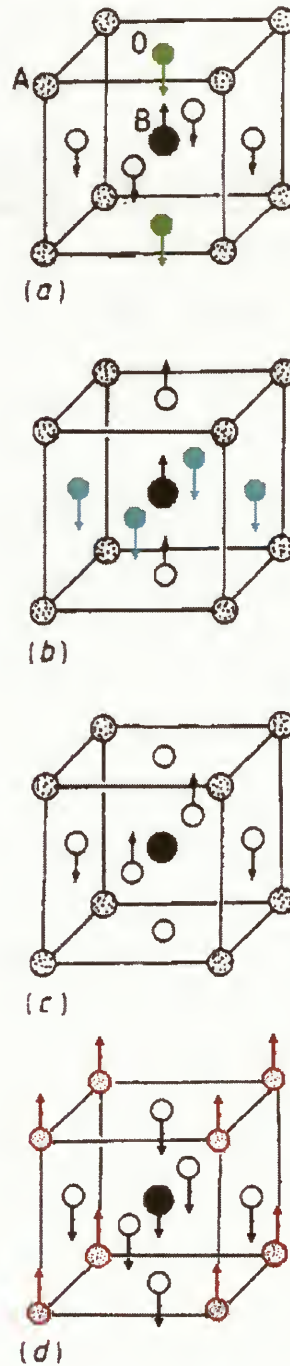


Figure 5.9: The optical phonon modes of the cubic perovskite structure  $\text{ABO}_3$ : (a) stretching; (b) bending; (c) inactive; (d) external. Two internal modes (stretching and bending) and one external mode are IR active [22].



Table 5.3: IR active modes for cubic SRO calculated using full potential LMTO linear response [20]

Frequency (cm <sup>-1</sup> )	Type of phonon mode
72	External Mode
225	Ru-O Bending Mode
604	Ru-O Stretching Mode

expected, but in orthorhombic perovskite 60 modes. Hence for the sake of simplicity, the cubic perovskite structure was considered. It was expected that the orthorhombic distortion would produce small splitting within the three main bands [22, 23].

Apart from two STO modes, three main groups of film modes can be seen in all the spectra of figures 5.4 and 5.5. A comparison of the frequency of the stretching mode of the perovskite listed in table 5.3 with the SRO spectrum of figure 5.4 or 5.5 suggests the mode at near 580 cm<sup>-1</sup> is probably the Ru-O stretching mode. Note that all of the spectra show a peak due to the Ru-O stretch phonon mode. In figure 5.10 the lowest panel,  $\omega_0$  of Ru-O stretch mode is plotted versus Mg content. The data of figures 5.10 and 5.11 comes from table 5.2. The Ru-O stretch mode frequency decreases as the amount of doped Mg increases. Note that this trend is quite similar to the VDF results shown in figures 5.4 and 5.5.

It is well known that  $\omega_0$  will depend on the crystal structure, especially on the bond strength. When bond strength decreases, the restoring force of the vibration mode decreases, resulting in a decrease of  $\omega_0$ . So data suggest that doping Mg reduce the



strength of Ru-O bond. The increase of width of Ru-O mode will increase Mg-doping is also reasonable.

The peaks near 300 cm<sup>-1</sup> are assigned to Ru-O bending modes. In figure 5.4, note that just SRO and Mg-doped SRO with  $x=0.05$  show a peak due to Ru-O bending mode near 280 cm<sup>-1</sup>. In all films there is a feature at 325 cm<sup>-1</sup>, but it appears stronger in the Mg-doped films. We are not sure about the type of this band, there is a chance that it may be due to Mg-O bending mode. But apparently by increasing Mg content (correlated with decreasing out-of-plane lattice parameter) this phonon peak becomes more symmetric. This may be related to changes in the RuO<sub>6</sub> octahedron or to growth of Mg-O bending modes at different frequency from the Ru-O bending modes. This mode should be explored further.

There is another feature near 670 cm<sup>-1</sup> in Mg-doped samples attributed to Mg-O stretch mode, because it is at higher frequency than the Ru-O stretch. By looking at figure 5.11, one can see that with increasing Mg doping,  $\omega_0$  of the Mg-O stretch mode remains at the same value, but the width of the peak as well as its strength are decreased when  $x > 0.05$ .

This investigation was aimed at checking the technique and also getting answer to this question that whether Mg<sup>2+</sup> would go to Ru or Sr site. Analysis of our data suggest that Mg<sup>2+</sup> goes to Ru site. Because both the bend and stretch modes of SRO are affected. Unfortunately the lower frequency external mode (Sr versus RuO<sub>6</sub>) is not observed in the frequency range studied. If Mg is going in to the Ru site only, it is expected that this mode will not split.

Note that the Ru-O and Mg-O stretch modes DL parameters for sample DM31 are different than for all the others especially the width of Ru-O stretch mode is so



---

much greater ( see figures 5.11, 5.10). This is probably due to the fact that DM31 is more Oxygen deficient than the other samples. ( see table 5.1).



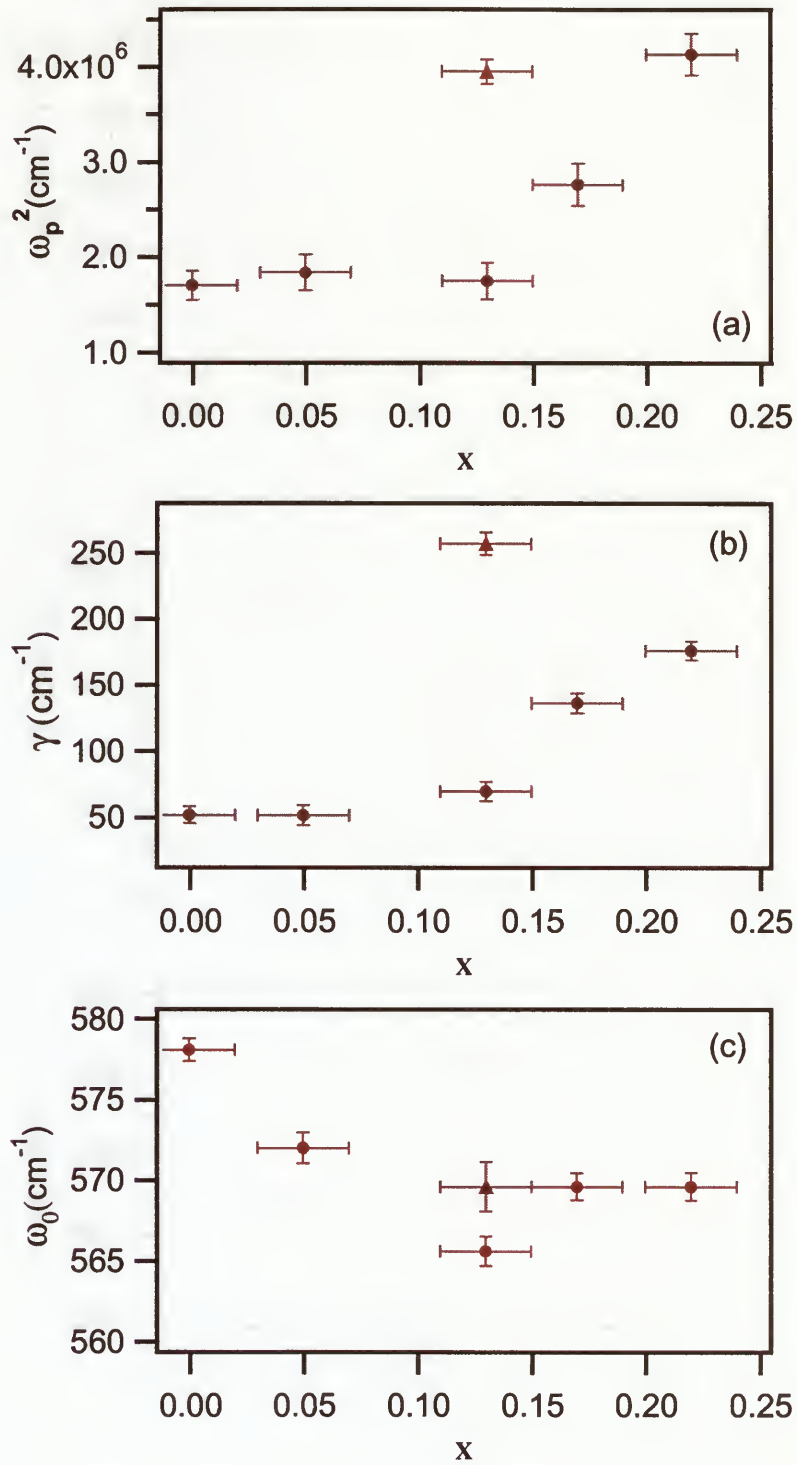


Figure 5.10: IR active mode frequency  $\omega_0$ , scattering rate  $\gamma$  and bonding strength  $\omega_p^2$  versus composition ( $X$ ) for Ru-O stretch mode. Triangle shape represents DM31 film.



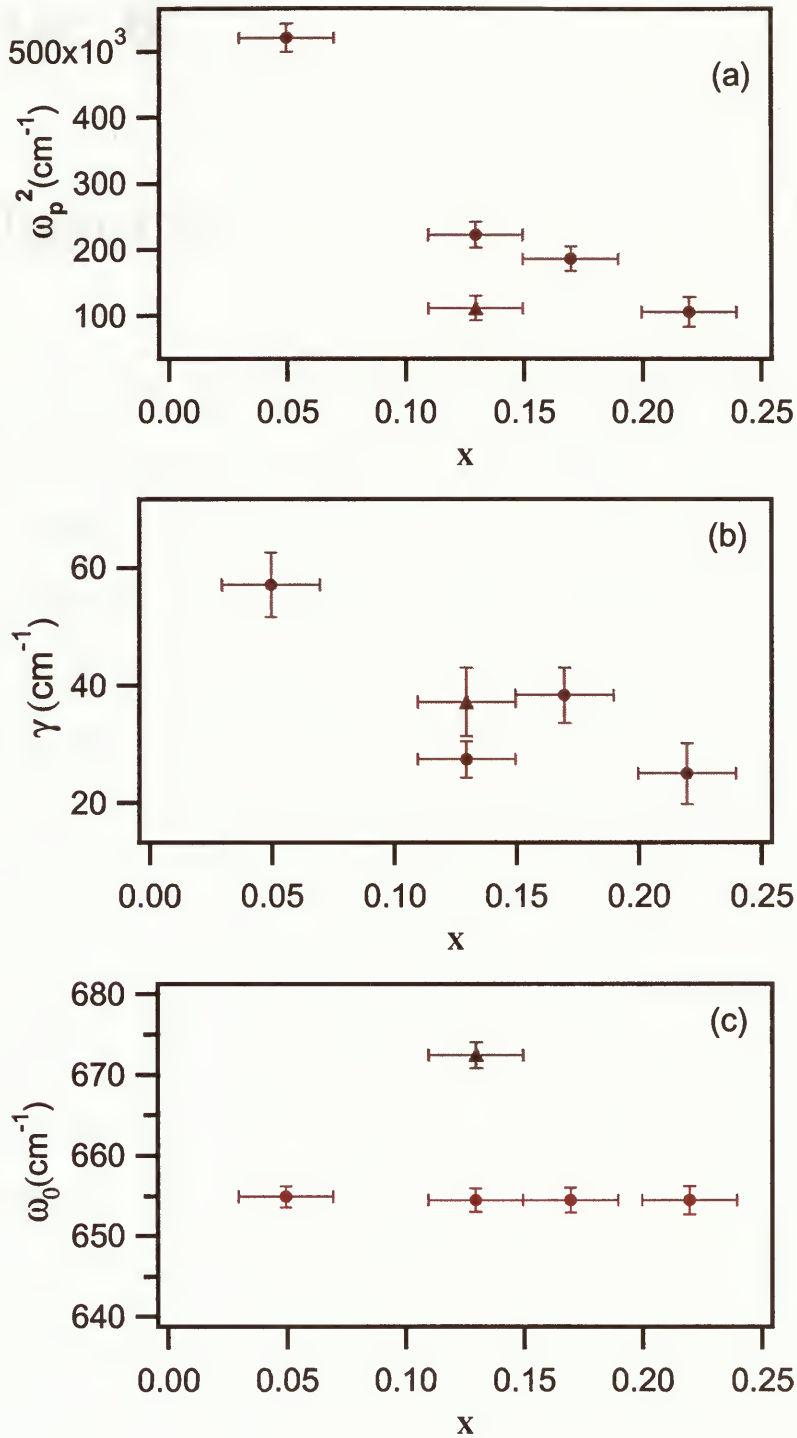


Figure 5.11: IR active mode frequency  $\omega_0$ , scattering rate  $\gamma$  and bonding strength  $\omega_p^2$  versus composition ( $X$ ) for Mg-O stretch mode in  $\text{SrMg}_y\text{Ru}_{1-y}\text{O}_{3-\delta}$  thin films. Triangle shapes represent DM31 film.



# Chapter 6

## Conclusions

Checking the technique of finding optical conductivity  $\sigma(\omega)$  by fitting reflectance spectra using VDF method was the first goal of this project. A program was written successfully to implement VDF fitting for both single crystals and thin films.

The VDF technique is based on Drude-Lorentz model. From Drude-Lorentz model fitting, we have got the same value for the low frequency optical conductivity results as DC measurements. Because the VDF is more flexible than DL method to fit all features of the reflectance spectra, it reveals splitting of some modes, which are not shown in Drude-Lorentz fitting.

However, it seems that VDF could not eliminate substrate's contribution from film conductivity results. Maybe our assumption for  $\epsilon_s$  is subject to error. The measured films were deposited on polished substrate but the dielectric function of polished and unpolished crystals may be slightly different this may be the reason that the substrate contribution could not be totally removed.

Furthermore, the comparison of the two different programs implementing VDF fitting shows that this technique has a uniqueness problem. But still the presence of vibrational modes near  $300\text{cm}^{-1}$ ,  $580\text{ cm}^{-1}$  and  $670\text{ cm}^{-1}$  cannot be disputed. In addition, Mg-doping decreases the number of free electrons and causes a midinfrared



bond to move to higher frequency.

The second goal of the thesis was to study Mg-doped  $\text{SrRuO}_3$  thin films. Previous uncertainty in chemical analysis left open the possibility that Mg is substituting into both Sr and Ru sites. All the conductivity spectra show a peak due to the Ru-O stretch phonon mode ( $\sim 580 \text{ cm}^{-1}$ ). This mode's frequency decreases as the amount of doped Mg increases, which is implied that doping Mg reduces the strength of Ru-O stretch bond. Also VDF analysis shows another feature at higher frequency ( $\sim 670 \text{ cm}^{-1}$ ) than the Ru-O stretch, attributed to Mg-O stretch mode. Furthermore, VDF fitting reveals splitting of bending modes. Since both the bend and stretch modes of SRO are splitting, VDF analysis lead us to conclude that  $\text{Mg}^{2+}$  goes to Ru site. Unfortunately, our data did not extend to low enough frequency to explore any splitting of the external mode, so we are still uncertain as to whether  $\text{Mg}^{+2}$  goes into  $\text{Sr}^{+2}$  site.



# Appendix A

## Preparing $\text{Sr}_{1-x}\text{Mg}_{x+y}\text{Ru}_{1-y}\text{O}_{3-\delta}$ thin films

$\text{Sr}_{1-x}\text{Mg}_{x+y}\text{Ru}_{1-y}\text{O}_{3-\delta}$  thin films were made by laser ablation on  $\text{SrTiO}_3$  (001) substrates in  $\text{O}_2$  atmosphere. A polycrystalline  $\text{SrRu}_{0.85}\text{Mg}_{0.15}\text{O}_3$  target was made by conventional solid-state reaction at  $1100^\circ\text{C}$  after mixing stoichiometric amount of  $\text{SrCO}_3$ ,  $\text{RuO}_2$  and  $\text{MgO}$ . The details of raw material mass ratios are given in table A.1.

Table A.1: Experimental raw material mass ratios for making  $\text{SrRu}_{0.85}\text{Mg}_{0.15}\text{O}_3$  [26]

Material	Mass ratio
$\text{SrCO}_3$	1
$\text{RuO}_2$	0.766
$\text{MgO}$	0.0409

$\text{SrTiO}_3$  (STO) is one of the most applicable substrates with a perovskite structure and the lattice parameters of  $a = b = c = 3.905\text{ \AA}$  [27]. Before deposition STO were cleaned using ultrasound in acetone and then ethanol. The substrates were fixed at around 3.5 cm of target. The films were grown by laser deposition using a XeCl laser



Table A.2: Thin film growth parameters

Sample Number	Target	Substrate Temperature°C	$P_{O_2}(mT)$	Pulses
DM29	$SrRu_{0.85}Mg_{0.15}O_3$	500	200	20000
DM30	$SrRu_{0.85}Mg_{0.15}O_3$	500	200	20000
DM31	$SrRu_{0.85}Mg_{0.15}O_3$	500	200	10000
DM33	$SrRu_{0.85}Mg_{0.15}O_3$	600	200	20000
DM34	$SrRu_{0.85}Mg_{0.15}O_3$	700	200	20000

\*Ru- deficient  $SrRuO_3$  target (precise stoichiometry unknown)

operating at  $\lambda = 308$  nm, 4Hz repetition rate and approximate energy density  $1 \text{ J cm}^{-2}$ . After deposition, all the samples were cooled to room temperature with  $P_{O_2} = 1.01 \times 10^5$  Pa.  $P_{O_2}$  refers to the total pressure in the PLD chamber. Table A.2 indicates all the thin film's condition in which they were made.

The diffraction patterns of  $Sr_{1-x}Mg_{x+y}Ru_{1-y}O_3$  (Mg-SRO) on STO have been determined by power x-ray diffraction (XRD). The data show that all samples were grown epitaxially with [001] perpendicular to the substrate face, same as pure SRO films grown on STO substrates.



# Appendix B

## $\text{Sr}_{1-x}\text{Mg}_{x+y}\text{Ru}_{1-y}\text{O}_{3-\delta}$ Samples Characterization

### B.1 RBS: Stoichiometry and Thickness

The stoichiometry of the films was explored using Rutherford backscattering (RBS). In addition to composition, RBS can yield information about film thickness. In the RBS measurement all spectra were collected at a total count rate less than 1000 counts  $\text{s}^{-1}$  using incident  $\text{He}^{2+}$  ions at 2 MeV.

Figure (B.1) presents the RBS spectrum of all five Mg-SRO samples. The arrow in each panel indicates the edge associated with Ru at the back of the film.

### B.2 Electrical and magnetic properties

In figure (B.2) the remanent magnetization versus temperature is illustrated for the all Mg-SRO thin film samples. The temperature dependence of the remanent magnetic moment of the films was measured using a Quantum Design SQUID magnetometer by first zero field cooling to 5K, then ramping the field to 5T and finally reducing the field



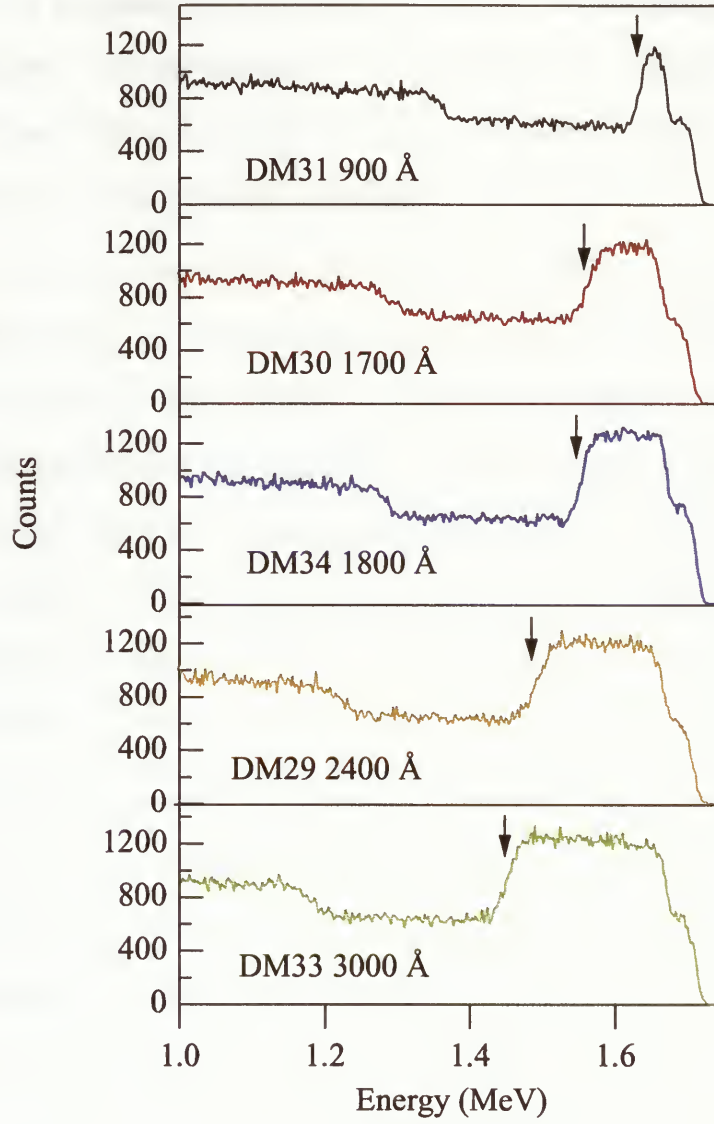


Figure B.1: RBS spectrum of all Mg-SRO samples. The arrow in each panel indicates the edge associated with Ru at the back of the film.



to approximately  $0 \pm 0.001$  T. This large field was chosen because the magnetization of SRO does not saturate at low fields [28]. As seen all the samples show evidence of ferromagnetism. But one may notice magnetization for DM31, the thinnest film, does not reach zero above  $T_c$  ( $\approx 160$  K) despite the others. It is not known why the magnetization is so large above  $T_c$  in DM31.

Figure (B.3) shows temperature dependent DC resistivity curves  $\rho(T)$  of the Mg-SRO thin films which was measured using the Van der Pauw technique. As seen in figure (B.3), except for DM34, the cusp in resistivity seen at the Curie temperature in pure SRO films has completely disappeared in all the samples. It seems that magnetic transition does not affect the transport properties of those samples. Sample DM34, which has the smallest lattice parameter of all Mg-doped samples, is metallic over the whole temperature range studied. Sample DM31, which has the largest lattice parameter, exhibits a change from insulating to metallic behavior.

The electrical and magnetic properties of the films vary systematically with the lattice parameters of the films. The comparison of figures (B.2) and (B.3) at 5K indicates that the larger lattice parameter correlates with more resistivity and smaller remanent moments. Similarly at room temperature there is a systematic decrease in resistivity with lattice parameter.



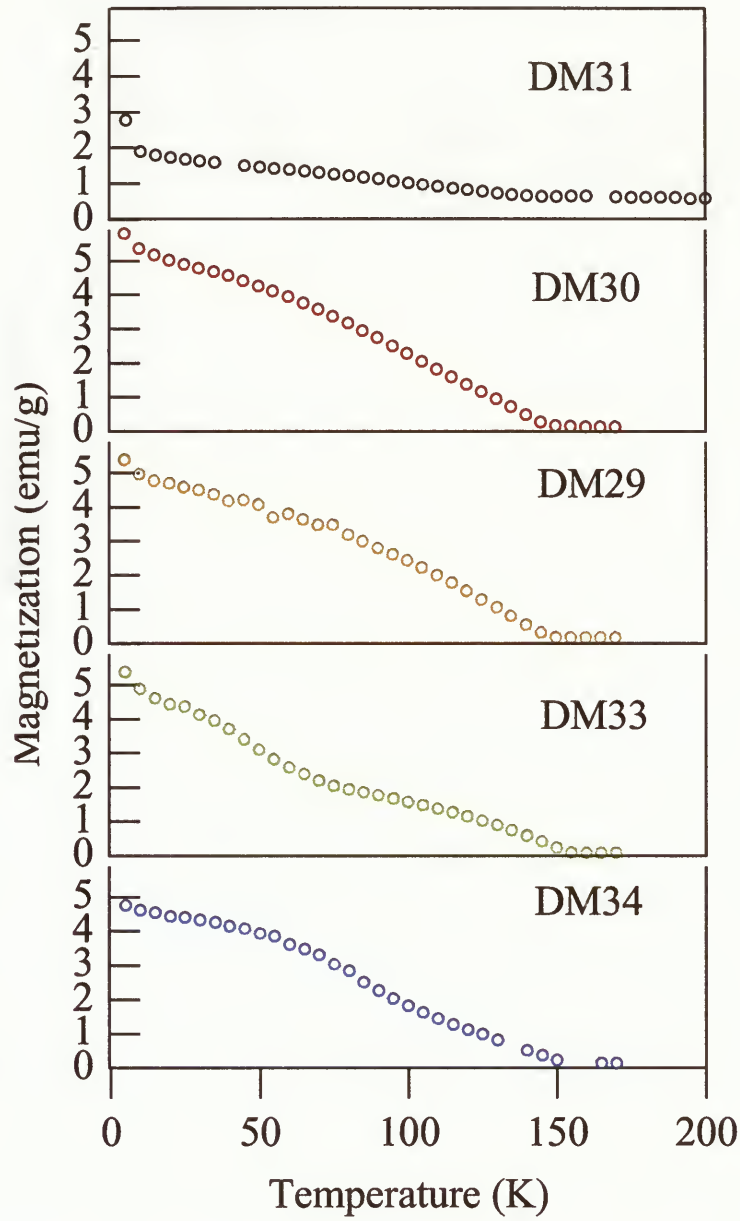


Figure B.2: Temperature dependent remanent magnetization of all samples



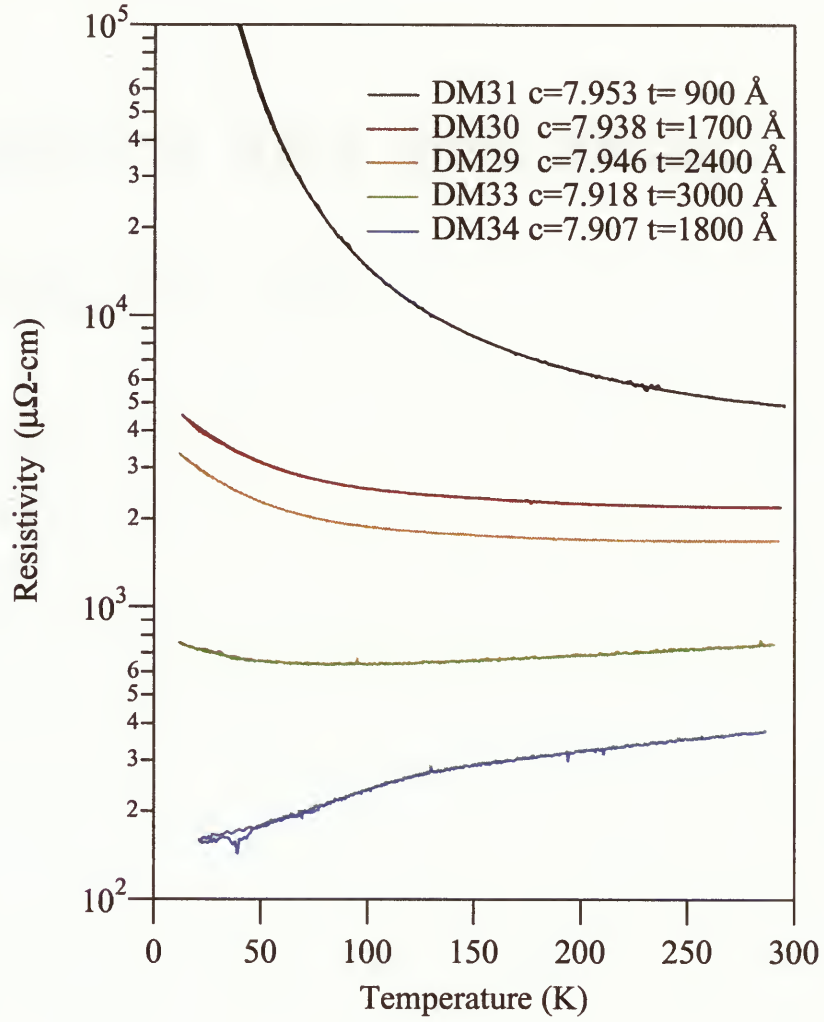


Figure B.3: Temperature dependent DC resistivity of the five Mg-SrO samples used in the reflectance measurement



# Appendix C

## Rutherford Back Scattering

### Method [29, 30]

Rutherford Backscattering (RBS) is based on collisions between atomic nuclei. It involves measuring the number and energy of ions in a beam which backscatter after colliding with atoms in the near-surface region of a sample at which the beam has been targeted. With this information, it is possible to determine atomic mass and elemental concentrations versus depth below the surface.

In this technique a high energy beam (2 to 4 MeV) of low mass ions (e.g.  $\text{He}^{++}$ ) is directed toward a sample. When a sample is bombarded, the vast majority of particles are implanted into the material and do not escape. This is because the diameter of an atomic nucleus is on the order of  $10^{-15}\text{m}$  while the spacing between nuclei is on the order of  $10^{-10}\text{m}$ . A small fraction of the incident particles do undergo a direct collision with a nucleus of one of the atoms in the upper few micrometers of the sample. This collision does not actually involve direct contact between the projectile ion and target atom. Energy exchange occurs because of Columbic forces between nuclei in close proximity to each other. However, the interaction can be modeled accurately as an elastic collision using classical physics.

The number of backscattering events that occur from a given element in a sample



depend upon two factors: the concentration of the element and the effective size (cross section) of its nucleus.

The energy of backscattered particles will depend on their incident energy and on the mass of the sample atom which they hit, because the amount of energy transferred to the sample atom in the collision depends on the ratio of masses between the ion and the sample atom. Thus, measuring the energy of scattered particles indicates the chemical composition of the sample.

When probing particles penetrate to some depth in a dense medium, projectile energy dissipates due to interactions with electrons and to glancing collisions with the nuclei of target atoms. This means that a particle which backscatters from an element at some depth in a sample will have measurably less energy than a particle which backscatters from the same element on the sample surface. The amount of energy a projectile loses per distance traversed in a sample depends on the projectile, its velocity, the elements in the sample, and the density of the sample material. This means that RBS can be used as a means to perform a depth profile of the composition of a sample.

Analysis of Rutherford backscattering (RBS) is often done by simulation, means by adjusting the parameters associated with the simulated structure, one can optimize the fit between the simulated and measured spectra.



# Bibliography

- [1] A. B. Kuzmenko, "Kramers-Kronig constrained variational analysis of optical spectra", *Rev. Sci. Instr.* **76**, 083108 (2005).
- [2] A. Callaghan, C. W. Moeller, and R. Ward, "Magnetic Interactions in Ternary Ruthenium Oxides" *Inorg. Chem.* **5** 1572 (1966).
- [3] D. J. Singh, "Electronic and magnetic properties of the 4d itinerant ferromagnet  $\text{SrRuO}_3$  " *J. Appl. Phys.* **79** 4818 (1996).
- [4] C. W. Jones, P. D. Battle, P. Lightfoot, and W. T. A. Harrison, "Structure of  $\text{SrRuO}_3$  by time of flight neutron powder diffraction" *Acta Cryst. C* **45** 365 (1989).
- [5] A. Kanbayasi "Magnetic properties of  $\text{SrRuO}_3$  Single Crystal" *J. Phys. Soc. Japan* **41** 1879 (1976).
- [6] P.B. Allen, H. Berger, O. Chauvet, and L. Forro, T. Jarlborg, A. Junod, B. Revaz, and G. Santi "Transport properties, thermodynamic properties, and electronic structure of  $\text{SrRuO}_3$ " *Phys. Rev. B* **53** 4393 (1996).
- [7] X.D. Wu, S.R. Foltyn, R. C. Dye, Y. Coulter, and R. E. Muenchausen, "Properties of epitaxial  $\text{SrRuO}_3$  thin films" *Appl. Phys. Lett.* **62** 2434 (1993).



- 
- [8] L. Klein, J. S. Dodge, T. H. Geballe, A. Kapitulnik, A. F. Marshall, L. Antognazza, and K. Char, "Perpendicular magnetic anisotropy and strong magneto-optic properties of SrRuO<sub>3</sub> epitaxial films" Appl. Phys. Lett. **66** 2427 (1995).
- [9] L. Miville, T. H. Geballe, L. Antognazza, K. Char, "Ti and Ca substitution in SrRuO<sub>3</sub> thin films by sequential deposition process" Appl. Phys. Lett. **70** 126 (1996).
- [10] D. A. Crandles, M. Reedyk, R. W. Schaeffer, A. E. Hultgren, R. Schlee, "Metal-insulator transition in the SrRu<sub>1-x</sub>Mg<sub>x</sub>O<sub>3</sub> system" Phys. Rev. B **65** 224407 (2002).
- [11] S. Perkowitz, L. S. Kim, and Z. C. Feng "Optical phonons in Cd<sub>1-x</sub>Zn<sub>x</sub>Te" Phys. Rev. B **42** 1455 (1990).
- [12] M. Fox. *Optical Properties of Solids*, Oxford University Press, New York, 2001
- [13] M. Dressel and G. Grüner. *Electrodynamics of Solids*, Cambridge University Press, Cambridge, 2002
- [14] J.N. Hodgson. *Optical Absorption and Dispersion in Solids*, Chapman and Hall LTD, London, 1970
- [15] F. Wooten, *Optical Properties of Solids* , Academic Press, New York, 1972
- [16] William H. Press, Saul A. Teukolsky, William T. Vetterling, Brian P. Flannery, *Numerical Recipes in C++ : The Art of Scientific Computing*, Cambridge University Press, Cambridge, 2002
- [17] D. A. Crandles, Mohammad Mehdi Yazdanian and F. S. Razavi, "Metal- insulator transition in Mg-doped SrRuO<sub>3</sub> thin films prepared by laser ablation" J. Phys. D: Appl. Phys. **39** 6 (2006).



- 
- [18] J. S. Lee, Y. S. Lee, and T. W. Noh, "Bond-length dependence of charge-transfer excitations and stretch phonon modes in perovskite ruthenates: Evidence of strong p-d hybridization effects" *Phys. Rev. B* **70** 085103 (2004).
- [19] Web Site: <http://optics.unige.ch/alexey/reffit.html>
- [20] S.K. Bose, Private communication based on technique.
- [21] A. F. Santander-Syro, R. P. S. M. Lobo, N. Bontemps, Z. Konstantinovic, Z. Li and H. Raffy, "Absence of a Loss of In-Plane Infrared Spectral Weight in the Pseudogap Regime of  $Bi_2Sr_2CaCu_2O_{8+\delta}$ " *Phys. Rev. Lett.* **88**, 097005 (2002).
- [22] S Tajima, A Masaki, S Uchida, T Matsuura, K Fueki and S Sugai, "Infrared reflectivity and electronic states in perovskite-type oxides  $La_{1-x}Sr_xFeO_3$  and  $La_{1-x}Sr_xCoO_3$ " *J. phys. C* **20**, 3469 (1987).
- [23] D.A. Crandles, B. Nicholas, C. Dreher, C.C. Homes, A.W. McConnell, B.P. Clayman, W.H. Gong and J.E. Greedan, "Optical Properties of highly-reduced  $SrTiO_{3-x}$ " *Phys. Rev. B*, **59**, 12842, (1999).
- [24] J. R. Klassen, *MSc Thesis*, (2004).
- [25] Web Site: <http://alpha400.ee.unsw.edu.au/krcho/DKEMAC98.pdf>
- [26] M. M. Yazdanian, *MSc Thesis*, (2004).
- [27] C. L. Chen, Y. Cao, Z. J. Huang, Q. D. Jiang, Z. Zhang, Y. Y. Sun, W. N. Kang, L. M. Dezaneti, W. K. Chu, and C. W. Chu, "Epitaxial  $SrRuO_3$  thin film on (001)  $SrTiO_3$ " *Appl. Phys. Lett.* **71** 1047 (1997).



- 
- [28] Kiyama Takashi, Yoshimura Kazuyoshi, Kosuge Koji, Mitamura Hiroyuki and Goto Tsuneaki, "High-Field Magnetization of  $\text{Sr}_{1-x}\text{Ca}_x\text{RuO}_3$ " J. Phys. Soc. Japan **68** 3372 (1999).
- [29] Web Site : <http://www.eaglabs.com/en-US/references/tutorial/rbstheo/cairtheo.html>
- [30] Web Site : <http://omega.ujf.cas.cz/vdg/methods-rbs.html>









